Design of Miniaturized Underwater Vehicle with Propulsions for Deep-sea Research Applications

by

Saeed A. Merza

A Thesis Presented in Partial Fulfillment
of the Requirements for the Degree
Doctor of Philosophy

Approved June 2014 by the
Graduate Supervisory Committee:

Deirdre Ruth Meldrum, Chair
Shih-Hui Chao
Praveen Shankar
Srikanth Saripalli
Spring Melody Berman

Arizona State University

August 2014

ABSTRACT

The ocean is vital to the health of our planet but remains virtually unexplored. Many researchers seek to understand a wide range of geological and biological phenomena by developing technologies which enable exploration of the deep-sea. The task of developing a technology which can withstand extreme pressure and temperature gradients in the deep ocean is not trivial. Of these technologies, underwater vehicles were developed to study the deep ocean, but remain large and expensive to manufacture. I am proposing the development of cost efficient miniaturized underwater vehicle (mUV) with propulsion systems to carry small measurement devices and enable deep-sea exploration. These mUV's overall size is optimized based on the vehicle parameters such as energy density, desired velocity, swimming time and propulsion performance. However, there are limitations associated with the size of the mUV which leads to certain challenges. For example, 2000 m below the sea level, the pressure is as high as 3000 psi. Therefore, certain underwater vehicle modules, such as the propulsion system, will require pressure housing to ensure the functionality of the thrust generation. In the case of a mUV swimming against the deep-sea current, a thrust magnitude is required to enable the vehicle to overcome the ocean current speed and move forward. Therefore, the size of the mUV is limited by the energy density and the propeller size. An equation is derived to miniaturize underwater vehicle while performing with a certain specifications. An inrunner three-phase permanent magnet brushless DC motor is designed and fabricated with a specific size to fit inside the mUV's core. The motor is composed of stator winding in a pressure housing and an open to water ring-propeller rotor magnet. Several ring-propellers are 3D printed and tested experimentally to determine their performances and efficiencies. A planer motion optimal trajectory for the mUV is determined to minimize the energy usage. Those studies enable the design of size optimized underwater vehicle with propulsion to carry small measurement sensors and enable underwater exploration. Developing mUV's will enable ocean exploration that can lead to significant scientific discoveries and breakthroughs that will solve current world health and environmental problems.

ACKNOWLEDGMENTS

As an ordinary high school student form Kurdistan, Iraq with the struggle to have a peaceful life, I was blessed with the chance to immigrate to the United States of America in 1999. I could not attend university right away due to financial issues that I faced in my first year in Phoenix, Arizona. However, if it were not for my family, who gave me the full support including financial and mortal supports, I would have not had the chance to start my education in my new country.

At first, I would like to thank all of my brothers and sisters (Ashwaq Ahmad, Bassam Saeed, Saman Merza and Saineb Ahmad) for their faith in me. I also would like to thank my friends for their encouragement and their confidence in me.

Most of all, I would like to give my gratitude to my advisors, Dr. Deirdre Meldrum, Dr. Shih-hui Chao, Dr. Praveen Shankar, Dr. Srikanth Saripalli and Dr. Spring Melody Berman. They patiently provided the vision, encouragement and advice necessary for me to proceed through the doctoral program and complete my dissertation. Their unflagging encouragement and serving is the best role models to me as a junior member of academia.

Finally, I would like to thank Arizona State University NEPTUNE fund for their generous support. And all the staff and students at CBDA, I'm grateful to join and be a part of the lab. Thank you for treating me as a friend and helping me to achieve my project. Special thanks to my colleagues, Jieying, Bo, Jia for discussion and consolation.

TABLE OF CONTENTS

Page

CHAPTER

CHAPTER Page

LIST OF TABLES

Table Page

LIST OF FIGURES

FIGURE Page

FIGURE Page

FIGURE Page

FIGURE Page

FIGURE Page

1. OBJECTIVE AND RESEARCH CONTRIBUTION

1.1. Objective

Earth is unique among the other planets due to the existence of water. The presence of the three states of water offers a suitable environment for life to exist. The ocean environments are inhabited by many microorganisms that fundamentally influence the ocean's ability to sustain life on Earth. In the past few decades, there has been an increasing effort to understand the ocean and its existing life forms. However, the ocean remains a mystery due to the lack of exploration technologies. Its harsh environment is complicated by the absence of breathable oxygen, high pressure, low temperature and water salinity making it challenging for human's to study. The goal of this study is to develop a miniaturized underwater vehicle for ocean exploration and to evaluate its feasibility and effectiveness by optimizing a variety of parameters.

The objectives of the project include the following: *i*) Minimize (miniaturized) the size of the underwater vehicle with propulsion while retaining its performance standards. The size of underwater vehicles is related to many parameters such as propulsion parameters, shape parameters, mission duration and onboard energy density. This objective will address those parameters and use their relations to push the overall size of the underwater vehicle to the minimum; ii) Design a propulsion system that can generate the required thrust for the miniaturized underwater vehicle (mUV). The propulsion can be integrated into the mUV without increasing its overall size. This objective will explain the design process of fabricating a custom three-phase brushless DC motor with permanent magnets rotor to generate the required rotor speed. *iii*) Insulate the vehicle and its components to function in ocean environment. The issue of corrosion plays a major role in underwater vehicle design due to the high water salinity. In addition, the deep ocean environment introduces a high ambient pressure; hence, many underwater vehicles cannot function properly. This objective will achieve an insulation method to protect the vehicle from those issues; *iv*) Design a propeller to maximizer thrust and efficiency. In general, underwater vehicle with propulsion requires a propeller to generate thrust. The performance of the propeller plays a major role in the overall vehicle speed and power efficiency. This objective will apply an improved method to design a propeller with high efficiency to generate the maximum thrust.

The purpose of this project is to study the possibility of miniaturizing underwater vehicles with some design constrains to function properly in an ocean environment. Figure 1-1 shows the summary of this thesis by following the design steps for the major components of the vehicle.

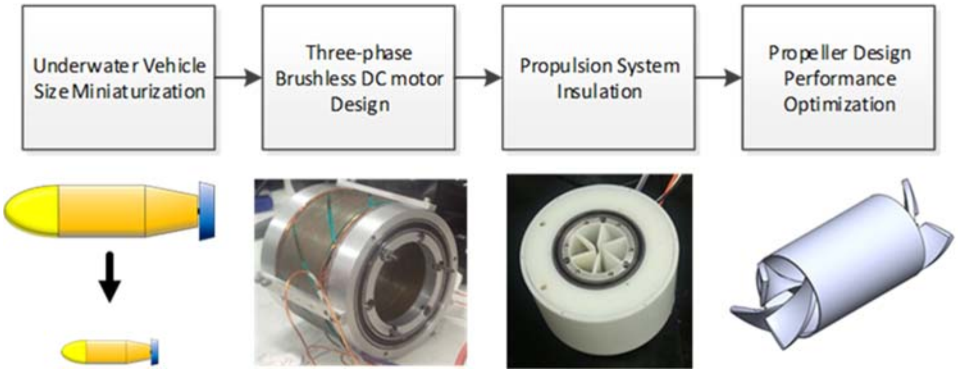

Figure 1-1 Flow diagram of the underwater vehicle design process.

1.2. Research Contributions

Underwater Vehicles is the key to exploring our ocean world in a much more efficient way. However, the ocean remains immense and the task to explore every part of it remains extremely difficult. This dissertation prospectus proposes the development of novel deep-sea miniaturized underwater vehicle as a method to enable the ocean discovery. The value of this proposal is emphasized by the innovative application of commonly available tools that are immediately relevant to researchers interested in developing miniaturized deep-sea compatible underwater vehicle.

Based on the projects results, all objectives have been successfully achieved. The scientific contribution of this research include: firstly, underwater vehicle size minimization with the constrain of traveling range. The task is to investigate the limit to push the size of the vehicle to the minimum while allowing a minimum traveling range performance. The result suggested that size of the vehicle depend mainly on the onboard energy density. Secondly, underwater brushless three-phase DC motor with permanent magnets was designed and fabricated to meet the demanded thrust generation of the propulsion system. The brushless motor was structured to occupy the core of the underwater vehicle. The significant of the brushless motor are: a) generating the required forward or backward thrust to permit motion to the underwater vehicle; b) the brushless motor has an inrunner rotor, which allow a new and easier method for stator electronic insulation; c) the whole propulsion module is independent and it can be integrated into other types of future underwater vehicles. Thirdly, the brushless motor was insulated using a new method, which inspired from the existing underwater propulsion insulation methods. This task suggests an insulation to the propulsion electronic parts such as the stator winding, energy sources (battery pack), electronic circuits and wiring. The non-electronic components were left outside the insulation such as the rotor, the permanent magnets and the propeller. Finally, the propeller was designed to induce the performance and maximize the overall vehicle efficiency. Blade element theory was applied to design several underwater propellers. Each propeller was experimentally tested to investigate the maximum thrust generated and its efficiency. The results suggested a maximum propeller efficiency of 46%.

In my learning curve for the past five and half years, I have presented my work progress, at least once a year, to the Biodesign Institute/Center for Biosignatures Discovery Automation group. In November 2012, I was invited by The Motor and Motion Association (SMMA) in St. Louis to attend a conference and present my designed underwater brushless motor. In addition, a journal paper is in progress for submission with Ocean Engineering Elsevier journal.

Merza, S. A., Thompson, A., Chao, J., & Meldrum, D. R. (2014). Brushless DC Motor with a New Pressure Housing Design Approach for Underwater Propulsion System. *Ocean Engineering*. In progress.

2. INTRODUCTION

The desire of understanding our ocean planet has increased drastically in the past two decades due to global climate changes (Karl & Trenberth, 2003) and the improvements of ocean technology systems (Kim, Choi, Lee, & jun Lee, 2014; Huang, Yang, Liu, & Schindall, 2013; Ruiz et al., 2012; Gracias & Santos-Victor, 2000). Therefore, many underwater vehicles were developed to perform certain tasks, which enable ocean measurements and discovery (Eriksen et al., 2001;Yoerger, Jakuba, Bradley, & Bingham, 2007; von Alt, 2003). However, before describing the underwater vehicle technologies, a step back must be taken to investigate the importance of the ocean and its influence on our planet and lives.

2.1. Why the Ocean?

The Ocean is the "engine" that drives weather-climate systems from the ocean basins onto the continents, directly affecting food production on land and the health of our planet. It covers nearly 71% of the planet and it is considered the largest habitant for life. Our understanding life's existence was based on sunlight (photosynthesis). However, the deep-sea has changed our prospective after the discovery of giant worms and clams near the hydrothermal vents. This type of life has a chemosynthetic-base, which suggests the possibility of life elsewhere in the cosmos (Maier-Reimer & Hasselmann, 1987; Tunnicliffe, 1992)

According to National Oceanic and Atmospheric Administration (NOAA) the biological productivity of the ocean plays a major role in global climate and carbon cycle which is the source of nearly 50 percent of the Earth's oxygen and 20 percent of the world protein supply (Field, 1998). In addition, the ocean species are also a potential basis of some medicines. (Tyson, Rice, & Dearry, 2004)

Life would not exist without our ocean. In fact, if planet Earth become without ocean, it would look like planet Mars where there is no life exist in the form earth life. Therefore, the ocean is vital to the health of our planet but remains virtually unexplored due to the hostility environment to the human life. The lack of breathable oxygen, high pressure encountered in the atmosphere, and unbearable low temperatures makes it unsuitable for humans to be present at the deep-sea level. Therefore, many researchers seek to understand a wide range of geological and biological phenomena by developing technologies that enable deep-sea exploration. (Gage & Tyler, 1992)

2.2. Where in the Ocean?

The Ocean Observatories Initiative (OOI) aims to extend power and bandwidth into the oceans. The OOI Regional Scale Nodes (RSN) has a Primary Infrastructure, which uses cables to distribute power and support communication from land to the sea in and around the Juan de Fuca Ridge. The cable is as 400km long and it provides a two-way communications between the land and the sea (see Figure 2-1) (Isern & Clark, 2003). Axial Seamount is the most robust volcanic system on the Juan de Fuca Ridge and it is seismically, magmatically, and hydrothermally active.(Tivey & Johnson, 1990)

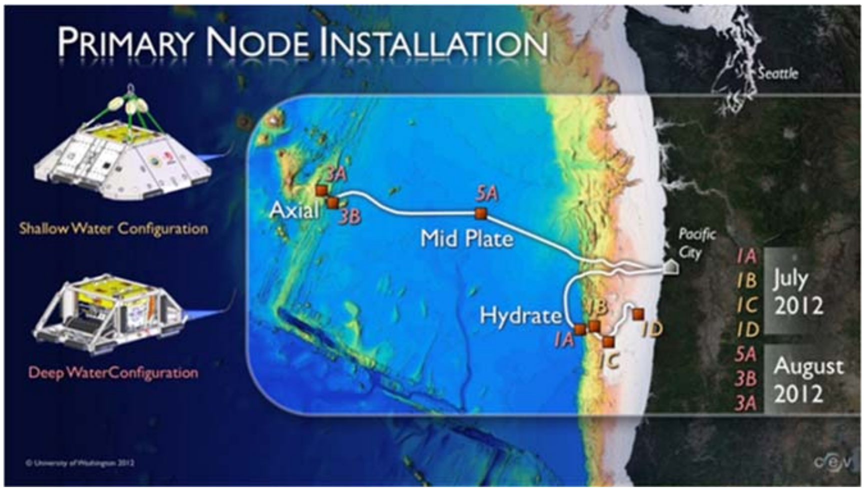

Figure 2-1 Primary Node locations on the Juan de Fuca Ridge to provide power and data communication.

2.3. Ocean floor future research vision

Our ocean discovery aim is to have high quantity of sensors mapping different areas of the ocean floor to preform simultaneous physical, chemical or biological measurements. The next step is to develop miniaturized Underwater Vehicles (mUV)'s with a mission to swim around the primary nodes or RSN and record measurements generated by the onboard sensors. Those mUVs onboard small sensors modules and small devices are designed to enable specific physical, chemical or biological measurements (such as temperature sensors, PH level sensor, Oxygen sensor, single cell gene analyze, etc.), within the targeted ocean floor. In addition, a network of mUVs can perform simultaneous physiological measurements to cover areas in a form of grids and nodes (see Figure 2-2). However, each individual mUV is limited with the amount of energy they require within one mission.

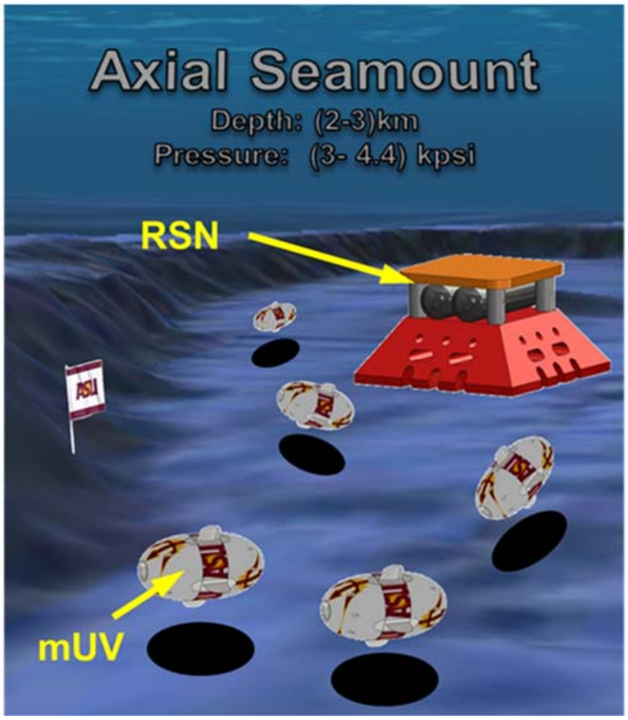

Figure 2-2 A network of underwater vehicles with sensors mapping the ocean floor to enable physical, chemical and biological discovery.

2.4. Types of underwater vehicles

Many researchers seek to understand a wide range of geological and biological phenomena by developing technologies, which enable deep-sea exploration. Of these technologies, underwater vehicles were developed to study the deep ocean. Many deep-sea underwater vehicles can be classified into two types.(Brown Jr & Hendrick, 1986; Yuh, 2000) The first type is manned underwater vehicles such as Deep-Submergence Vehicle (DSV). For example, Alvin (DSV) is a manned deep-sea research submersible. It dives 4.5 km below the ocean surface and travel at a maximum speed of 2 knots. Its size is about 7.1 m x 2.6 m x 3.7 m and it weight about 17 tons. In addition, Alvin can have two scientists and one pilot onboard.(Mavor, Froehlich, Marquet, & Rainnie, 1967) The second type is unmanned underwater vehicles, which are known as Autonomous Underwater Vehicle (AUV), and Remotely Operated Vehicle (ROV). AUVs are robots, which do not require input from an operator. Sentry (AUV), for example, was designed to operate at depth of 5 km below the ocean surface and travel at a maximum speed of 2.5 knots. Its specific task is to carry devises for sampling and measuring purposes.(Martin, Whitcomb, Yoerger, & Singh, 2006; D. Yoerger, Bradley, Martin, & Whitcomb, 2006) Sentry's dimension is 1.8 m x 2.2 m x 2.9 m. On the other hand, ROVs are tethered underwater robot vehicles. This type of robot is usually operated by an operator on land or in the air. For example, Jason (ROV) was design to access the deep ocean without leaving the deck of a ship. Its dimension is 1.8 m x 2.2 m x 2.9 m and its maximum traveling speed is 1.5 knot (see Figure 2-3).(D. R. Yoerger & Newman, 1986; D. R. Yoerger, Newman, & Slotine, 1986; D. R. Yoerger, Von Alt, Bowen, & Newman, 1986) Most of these types of deep-sea underwater vehicles were developed to explore the ocean. However, most of them are limited in their exploration capabilities, big, expensive and complicated to make and deploy.

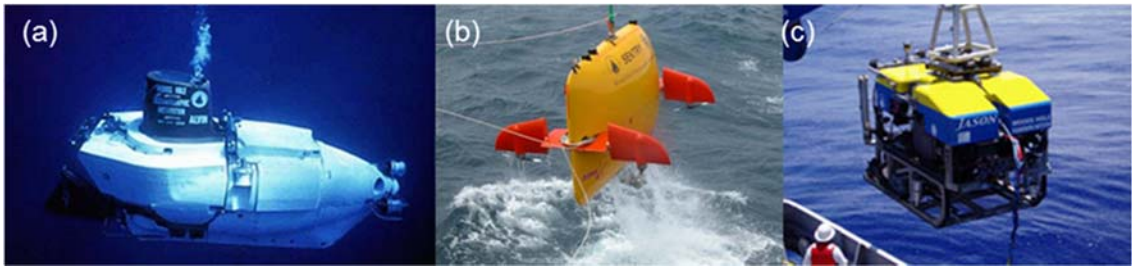

Figure 2-3 Underwater vehicles to explore the deep ocean. (a) Alvin. (b) Sentry. (c) Jason.

2.5. Unmanned underwater vehicle design philosophy

Most underwater vehicles were designed to fulfill a specific mission task. Unmanned underwater vehicle should be capable of performing a task that human cannot do. However, in most cases, cost becomes a factor where unmanned underwater vehicles overall cost is cheaper or safer than human dive. In the case of deep-sea research, unmanned underwater vehicles are the ideal technology selection. This is because of the high incompatible pressure that human cannot stand within the deep-sea environment.

The unmanned underwater vehicle design structure must meet the criteria that the missions demand. Most importantly, part of the vehicle space must be detected to hold a payload. In addition, for some measurement devices requires a dry pressure housing space to insure proper functionality. (T. Hyakudome, 2011)

The unmanned underwater vehicle should be made in the simplest form. The vehicle should not require team of engineers and programmers to operate the vehicle. The vehicle should have a simple interface where a technician with basic computer skills can operate it.

2.6. Underwater vehicle system and components

The most basic underwater vehicle must have some kind of navigation system, propulsion system and a dry, watertight environment to house onboard components. (Poole & Clower, 1996)

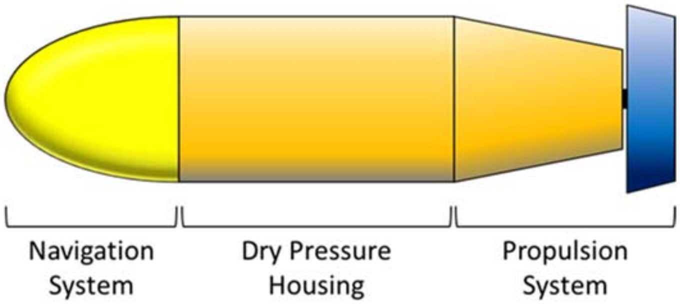

Figure 2-4 Basic componants of unmanned underwater vehicle.

Underwater navigations can be classified into two classes. At the water surface, GPS systems can be used to access highly accurate position data worldwide with up to one-meter error. However, GPS radio frequency signal do not penetrate through water. (Schelleng, Burrows, & Ferrell, 1933)Therefore, other positioning methods can be used such as inertial motion unit (IMU) and Doppler velocity log (DVL). The IMU can determine the vehicle orientation and the VDL can measure the vehicle speed relative to the sea floor.(Rowe & Young, 1979) However, DVL systems are expensive and may not be ideal for many applications. Other types of underwater navigation, while still expensive, includes long baseline navigation (LBL). (Larsen, 2000) LBL is one of the underwater acoustics positioning systems, which use a network of sea floor, mounted baseline transponders as a reference points for navigation. Remotely operated vehicles (ROV) can be navigated through visual landmarks or a compass. (Ramírez, Vásquez, Gutiérrez, & Flórez, 2007)

Propulsion system is another important component of underwater vehicles. There are different types of underwater propulsions that generate thrust to provide motion to the vehicle. Propeller base propulsion is considered the most efficient method for underwater long traveling range (Bellingham et al., 2010).

2.7. Current small underwater vehicles

The Autonomous Systems and Controls Laboratory (ASCL) at Virginia Tech focus on novel research contribution toward autonomous systems control, estimation, decision theory, the design of novel hardware, and the practical art of operating advance vehicles in the field. ASCL designed four autonomous underwater vehicles with different specifications. All four considered small and compact with a special specifications. The four AUV's principal characteristics are shown in Table 2–1. (Arafat, Stilwell, & Neu, 2006; Briggs, 2010; Petrich & Stilwell, 2011)

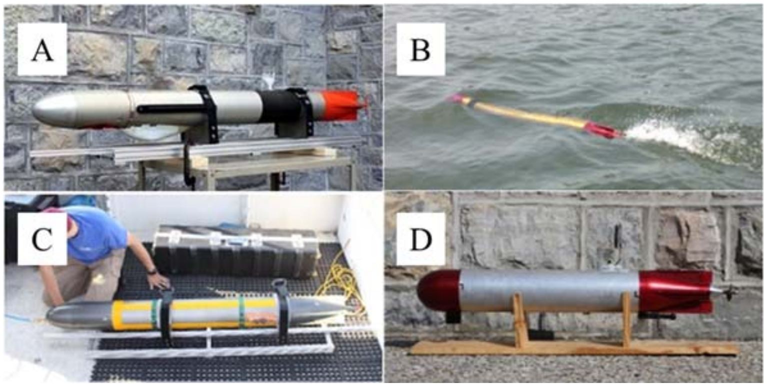

Figure 2-5 Current existing AUVs. (A) 690 AUV. (B) High Speed AUV. (C) Self-Mooring AUV. (D) 475 AUV.

Table 2–1

Small Autonomous Underwater Vehicles desiged by Virginia Tech ASCL.

AUV Name	Size (Length, Diameter) in inches	Max Depth in meter	Speed in knots	Endurance in hours	Description
690 AUV	(81,6.9)	500	4	24	Bathymetric surveys
High Speed AUV	(36,3)	N/A	>15	N/A	Small and fast
Self-Mooring AUV	(89,6.9)	500	4	N/A	Mooring itself on the seafloor
475 AUV	(34,4.75)	N/A	3	8	Enable research and development objectives

3. MINIATURIZED UNDERWATER VEHICLE DESIGN

Small ocean instrument platforms offer a much higher measurement resolution in space and time. (Dickey, 1991; Eriksen et al., 2001) In many cases, ocean research is not constrained by the overall underwater vehicle size. However, for some specific research purpose, the overall size of the underwater vehicle plays a major role in the discovery mission. (Behar, Bruhn, & Carsey, 2003) For example, astrobiology researchers seek to study the microbial ecosystems under the ice in Earth's Polar Regions. In many cases, creating large opening is required to allow access to the water to enable benthic studies. Smaller size underwater vehicles can enable discovery in tiny places were large vehicle cannot. In some underwater research cases, multiple vehicles are necessary to perform simultaneous sensor measurements within different nearby areas. The cost of designing, fabricating and deploying underwater vehicles could play a major factor. Therefore, the size of each robot vehicle will be optimized to reduce ocean specific material costs. However, each robot must have the capability of carrying sensor devices (payloads), travel long ranges, be energy efficient and rechargeable, controllable, stable and easy to develop.

Several small underwater deep-sea sensors devices were available to measure physical and chemical parameters such as temperature, pH level and oxygen concentration. Miniaturized underwater vehicles were needed to carry the sensors around the ocean and record data to enable ocean discovery.

3.1. Energy sources and limitations

In many cases, energy source is the fundamental factor for deep-sea underwater devices. For most devices, the lifetime of operation is limited by the energy storage. There are three main energy types such as nuclear fusion, chemical and electrochemical. (Bradshaw, Hamacher, & Fischer, 2011; Winter & Brodd, 2004; Yang et al., 2011) Fusion batteries have the highest energy density. However, they are not compact and dangerous due to spew radioactive materials. The second highest energy density is the chemical energy type. However, the chemical energy type requires oxygen for combustions and is not suitable for ocean environment. Electrochemical energy type is the lowest energy among these sources. However, there are several advantages of this type of energy storage. First, they are clean and green energy. Second, it can be easily converted to other forms of energy. Third, they are inexpensive. Fourth, they can be rechargeable for several usage cycles. Most importantly, they can be easily transmitted to various location conveniently and efficiently. (Chalk & Miller, 2006) Based on these factors, the electrochemical energy is the best choice for underwater application. In addition, Li-ion batteries are the most common method of energy source for long traveling underwater vehicles, (see Figure 3-1). (Bradley, Duester, Liberatore, & Yoerger, 2000) In addition to the recharging ability, they can be enclosed with oil to protect it from the high pressure and the saltwater. (T. Hyakudome, Yoshida, Ishibashi, Sawa, & Nakamura, 2011)

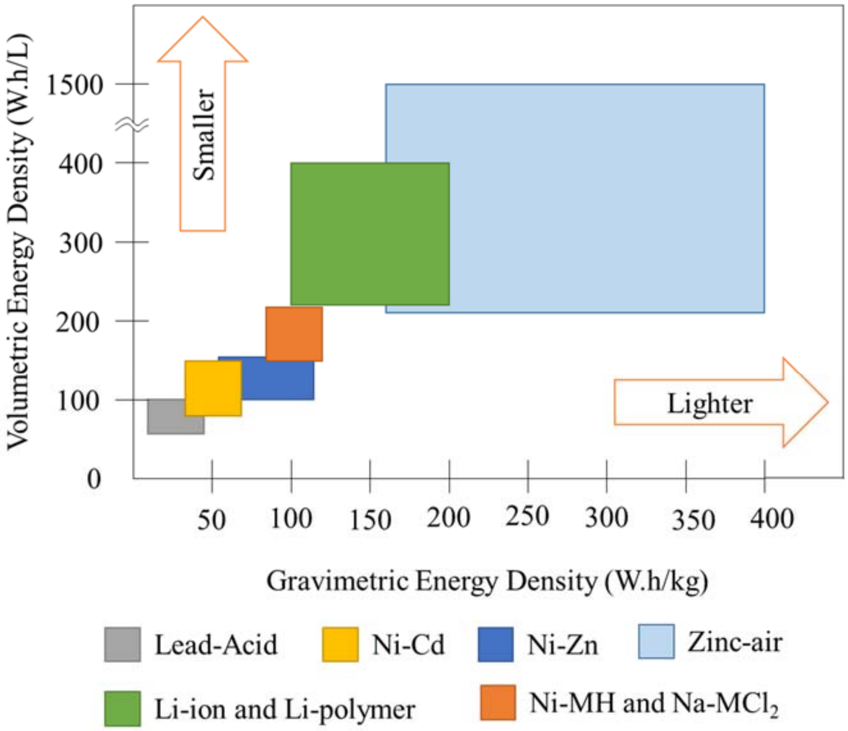

Figure 3-1 Energy density of several battrey technologies.

3.2. Underwater vehicle size optimization

The mean ocean current speed near the sea floor and west of Oregon (depth between 2700 m to 2900 m) is about 2 cm/s with a maximum speed of 6 cm/sec. The mean current speed from depth 725 m to 1700 m, range from 5 to 20 cm/s with a maximum of 20-40 cm/s depend on the water depth. (Korgen, Bodvarsson, & Kulm, 1970)

There are limitations associated with the size of the mUV which can lead to certain challenges. Beside the salinity of the ocean water, the pressure at the seafloor is usually high. For example, 2000m below the sea level, the pressure is as high as 3000psi.

Therefore, certain mUV component modules, such as the propulsion system, will require pressure-proof housing and corrosion resistance materials to ensure the functionality of the mUV. The most critical and challenging step of developing a mUV is to overcome the ocean current against which the mUV swims against.

Therefore, the size of the mUV is limited by the energy density. For example, the smaller the propeller, the more power (i.e. larger battery) is required to overcome the ocean current. However, minimizing the battery size also requires a larger propeller. Therefore, the mUVs propellers and the batteries must be developed at optimum sizes (see Figure 3-2).

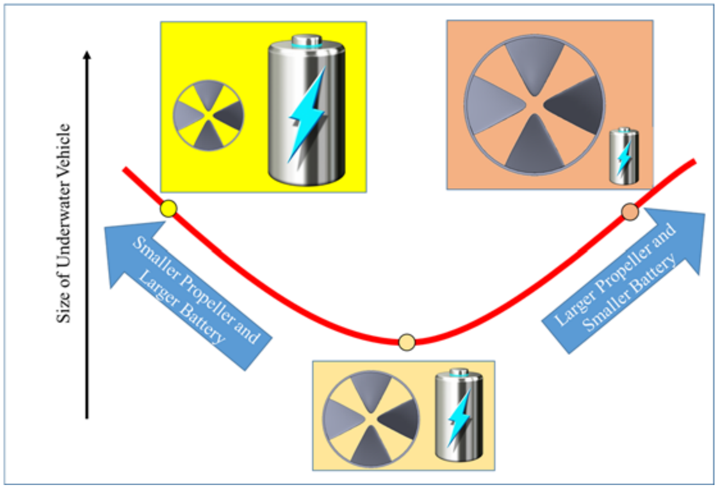

Figure 3-2 Vehicle overall siz as the sum of propeller size and battery size.

In order to complete this optimization, specific underwater vehicle design principles and structure must be applied. For a long-range traveling underwater vehicle, a torpedo shaped vehicle is the most common choice to improve the aerodynamic stability of the vehicle and to minimize drag. Furthermore, the propulsion system of the vehicle can be designed such that the driving motor is imbedded to the vehicle core. This allows easier process to insulate the motor stator and its electronic circuits to prevent from direct contact to the highly pressurized ocean water.

The miniaturized underwater vehicle is composed of three independent sections. First, the front section is dedicated to carrying ocean measurement devices such as a camera, temperature measurement device, biological cell/bacteria analyzers (PCR), etc. Second, the propulsion system occupies the middle section of the vehicle. Finally, the rear section of the vehicle is reserved for the maneuvering system. Figure 3-3 demonstrates the schematics of the vehicle.

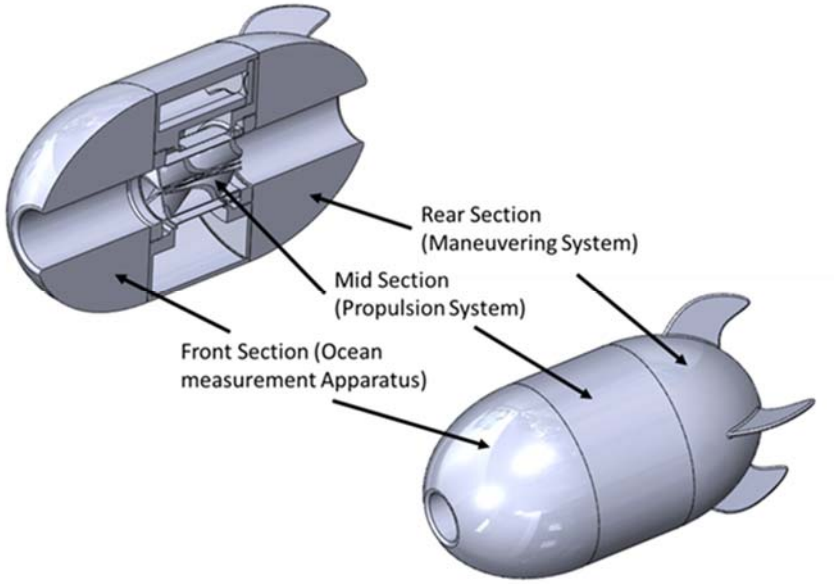

Figure 3-3 Miniaturized Underwater Vehicle divided into three independent major sections.

3.2.1. Continuous optimization problem

There are three major components such as the motor-thruster, battery and hotel load which adopt the overall underwater vehicle size. The frontal diameter of the vehicle (*D*) and the propeller diameter (*d*) are the two factors that determinate the traveling range and performance of the underwater vehicle. In addition, the length of the vehicle can be represented as direct proportional function of the mUV frontal diameter (for example, 2*D*). Therefore, the size of the vehicle can be represented with the two parameters *D* and *d* (see Figure 3-4).

$$V_{mUV} = \frac{\pi}{3}\left(D^2 - d^2\right)^{3/2}. \tag{3.1}$$

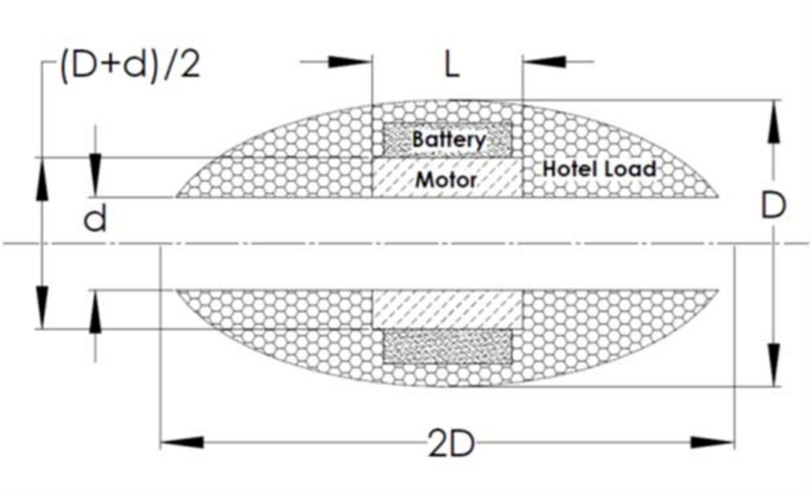

Figure 3-4 Schematic figure of the deep-sea mUV, which shows the structure of the vehicle with dimensions.

The hollow cylindrical motor size is part of the mUV overall size. I can assume a motor with a length *L* that has an outer diameter of the average length of the propeller diameter *d* and the mUV outer diameter *D*. This assumption is appropriate to insure the ability of the motor to fit inside mUV.

$$V_M = \frac{\pi L}{4}\left[\frac{(D+d)^2}{4} - d^2\right]. \tag{3.2}$$

The size of the battery can be represented as the ratio of the watt-hour (Power *P* and time *t*) to the energy density E_{VB}.

$$V_B = \frac{Pt}{E_{VB}}. \tag{3.3}$$

The extra space known as Hotel Load or Payload volume V_H such as flotation materials, housing materials and dead volumes can be represented as a fraction of the overall volume of the vehicle V_{mUV}.

$$V_H = \alpha V_{mUV}, \qquad 0 < \alpha < 1. \tag{3.4}$$

Therefore, the overall volume of the mUV can be expressed as the sum of all three volumes V_M, V_B and V_H,

$$V_{mUV} = V_M + V_B + V_H. \tag{3.5}$$

By substituting the equations (3.1), (3.2), (3.3), and (3.4) into equation (3.5) I get,

$$\frac{\left[\frac{\pi L}{4}\left[\frac{(D+d)^2}{4} - d^2\right] + \frac{Pt}{E_{VB}}\right]}{(1-\alpha)} = \frac{\pi}{3}\left(D^2 - d^2\right)^{3/2}. \tag{3.6}$$

The power of the *mUV* can be represented as the output power of the motor times the efficiency η.

$$P = \eta k_T I \omega, \tag{3.7}$$

where k_T is the motor torque constant, I is the motor rated electric current and ω is the rotation speed of the rotor.

I can use the propeller thrust force F_T equation and the drag force F_D equation to relate the propeller speed to the vehicle speed.

$$F_D = \frac{1}{2}\rho U^2 C_D A, \tag{3.8}$$

$$F_T = C_T \rho \omega^2 d^4, \tag{3.9}$$

where ρ is the fluid density, C_D is the drag coefficient, A is the frontal surface area and C_T is the thrust coefficient.

In steady state motions, assuming no external hydrodynamics effects and laminar flow, the two forces are equal. Therefore, the relation between the mUV velocity U and the propeller speed ω is,

$$\omega = \frac{UD}{2d^2}\sqrt{\frac{\pi C_D}{2C_T}}. \tag{3.10}$$

Substituting equations (3.10) into (3.7) lead to,

$$P = \frac{\eta k_T IUD}{2d^2}\sqrt{\frac{\pi C_D}{2C_T}}. \tag{3.11}$$

The frontal area A of the mUV can be expressed as $\pi D^2/4$. I combine equations (3.6) and (3.11) to get the relations between the mUV propulsion and battery parameters and its shapes parameters.

$$\frac{\left[\frac{\pi L}{4}\left[\frac{(D+d)^2}{4}-d^2\right]+\frac{\eta k_T IUDt}{2d^2 E_{VB}}\sqrt{\frac{\pi C_D}{2C_T}}\right]}{(1-\alpha)}=\frac{\pi}{3}\left(D^2-d^2\right)^{3/2}. \tag{3.12}$$

Equation (3.12) represents the equality constraint subject to the domain,

$$\min D^2+d^2, \tag{3.13}$$

with the inequality constraint,

$$D>d>0. \tag{3.14}$$

The constant α can be approximated by using the following buoyancy balance equation.

$$F_{net}=\left(m_M+m_B+m_H\right)g-\rho V_{mUV}g, \tag{3.15}$$

where F_{net} is the buoyancy force pointing up or down, m_M is the mass of the motor, m_B is the mass of the batteries, m_H is the mass of the hotel load and g is the gravitational acceleration.

The mass of the battery can be calculated from its specific energy ($m_B=Pt/E_{mB}$). The mass of each other sections can be computed using the product of its equivalent density and the volume ($m=\rho V$). To make the mUV neutrally buoyant, the net force must equal to zero. Therefore, after using equations (3.1), (3.2), (3.3), (3.4), and (3.11) equation (3.15) becomes,

$$\frac{\pi \rho_M L}{4}\left[\frac{(D+d)^2}{4}-d^2\right]+\frac{\eta k_T IUDt}{2E_{mB}d^2}\sqrt{\frac{\pi C_D}{2C_T}}=\frac{\pi}{3}(\rho-\alpha\rho_H)(D^2-d^2)^{3/2}, \tag{3.16}$$

3.3. Results

Before minimizing the continuous optimization problem equations (3.12), (3.13), (4.2), and (3.16) require certain parameters, which were determined by assumptions, lookup tables and preliminary experiments. Table 3–1 represents the value of each parameter needed for equation (3.12) and (3.16).

Table 3–1

Miniaturized Underwater Vehicle parameters.

Parameter	Notation	Value	Unit
Battery Volumetric Energy Density	E_{VB}	1	MJ/L
Battery Gravimetric Energy Density	E_{mB}	0.37	MJ/kg
Vehicle Speed	U	1	m/s
Swimming Time	t	24	hour
Electric Current	I	2	A
Motor Length	L	2.625	inch
Motor constant	k_T	0.015	N.m/A
Motor Equivalent Density	ρ_M	2700	Kg/m^3
Efficiency	η	0.30	unitless
Drag Coefficient	C_D	0.267	unitless
Thrust Coefficient	C_T	0.10	unitless

After plugging the parameter from Table 3–1, equations (3.12), (3.13), (3.14), and (3.16) were solved using online Wolfram Alpha computational knowledge engine. The result suggested a vehicle diameter of 0.154 m and propeller diameter of 0.041 m.

Using the parameter from Table 3–1, the relation between *D* and *d* were plotted as shown in **Error! Reference source not found.**. In this case, the outer diameter of the mUV cannot be smaller than about 6 inch (0.153 m). Therefore, the appropriate propeller size is 1.575 inch (0.04 m).

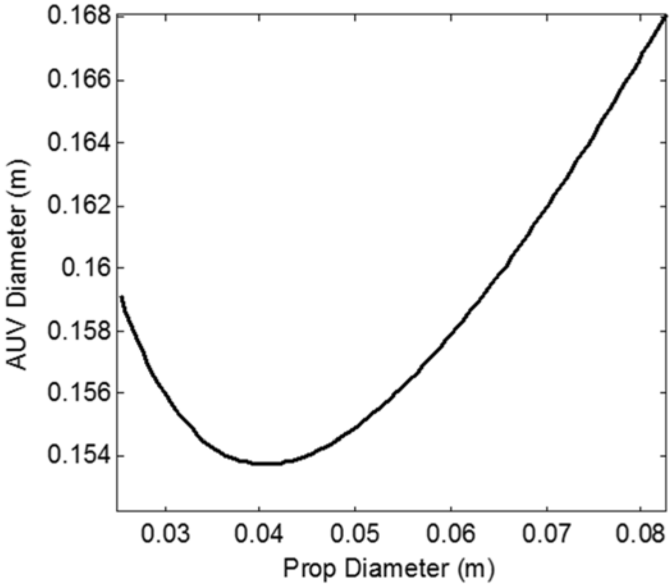

Figure 3-5 The relation between the propeller diameter and the mUV outer diameter. Based on the chosen and calculated parameters, the smallest AUV outer diameter is about 15.3cm (6in) which corresponds to a propeller diameter of 4.0cm (1.575in).

3.4. Discussion and conclusion

The size of the mUV was determined to have a diameter of six inches and twelve inches in length. The ring-propeller diameter cannot be smaller than 1.6 inches otherwise the vehicle will not meet the required performance. These results were determined through the analysis, which consider a linear motion with the assumption of continuous maximum vehicle speed with no additional disturbance to the system. In addition, the energy source of the mUV is fully dedicated to the motor system only. Heat and power losses were not taking into the account in order to simplify the miniaturization process.

It is important to realize that the mUV outer diameter must be greater than the ring-propeller diameter. This will lead the increase in the vehicle rooming size, which leads to an easier way to include extra components or extra energy sources such as batteries. However, the ratio of the mUV outer diameter to the ring-propeller squared diameter influence the relation between the ring propeller speed and the vehicle forward speed. This leads to a chance in the vehicle performance and range shortage.

The future of this type of miniaturized underwater vehicle can occupy not only our ocean but it might be a method to discover outer space planets, which contains liquid water such as Europa. The mUV can also be a module to integrate into a larger underwater vehicle system to act as the propulsion system source.

4. VEHICLE EQUATION OF MOTIONS

The model base of the vehicle can be described using the equation of motion. Assuming naturally buoyant and a linear motion for the mUV with fins, using a propeller on a torpedo shaped vehicle and no external flow disturbances. The force and moment acting on the mUV are shown in Figure 4-1.

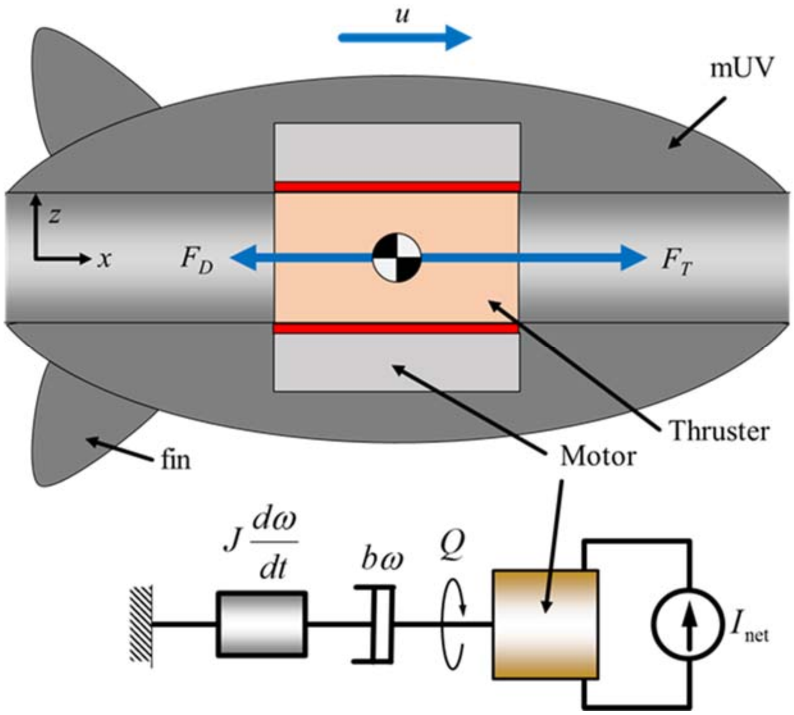

Figure 4-1 mUV and propulsion system schematics with forces acting on it.

Therefore, the equation of the propeller speed ω driven by the motor with a motor constant K_T is,

$$J\frac{d\omega}{dt} = -b\omega - Q + K_T I_{net} \tag{4.1}$$

where J is the moment of inertia along the x-axis, b is the bearing damping coefficient, Q is the propeller torque and I_{net} is the net electric rated current applied to the motor.

Due to the thrust F_T generated by the propulsion system, the mUV with a mass m will travel at a speed u.

$$m\frac{du}{dt} = -F_D + F_T \tag{4.2}$$

where F_D is the drag coefficient of the vehicle.

Assuming no cavitation, neglect frictional losses, incompressible fluid, no gravity effects, and perfect propeller symmetry the parameter Q, F_T and F_D can be expressed as,

$$Q = C_Q \rho \omega^2 d^5 , \tag{4.3}$$

$$F_T = C_T \rho \omega^2 d^4 , \tag{4.4}$$

$$F_D = \frac{1}{2} C_D \rho u^2 A , \tag{4.5}$$

where C_Q, C_T and C_D are the propeller torque constant, propeller thrust constant and mUV drag constant, respectively.

The equations (4.3), (4.4) and (4.5) will give positive values since they represent the magnitude of the torque and forces. However, in order to incorporate the direction of the torque and the forces, the signs of the propeller rotation speed and the mUV velocity must be carried along the Ordinary Differential Equations (ODE) shown in equation (4.1) and (4.2). Therefore, the square terms of u and ω can be broken down as the product of itself and its absolute value (i.e. $u^2 = u \cdot |u|$ and $\omega^2 = \omega \cdot |\omega|$).

The yaw of the mUV can be controlled by the fins. This will enable the mUV to move within x-axis and y-axis. Figure 4-2 shows the lift force generated by the fin and acting on the mUV. According to (Prestero, 2001), the lift force can be calculated using blade element theory.

$$F_L = \frac{1}{2}\rho C_L H\delta u^2, \tag{4.6}$$

where C_L is the lift coefficient of the fin, H is the surface area of the fin, and δ is the angle between the fin and forward axis of the mUV.

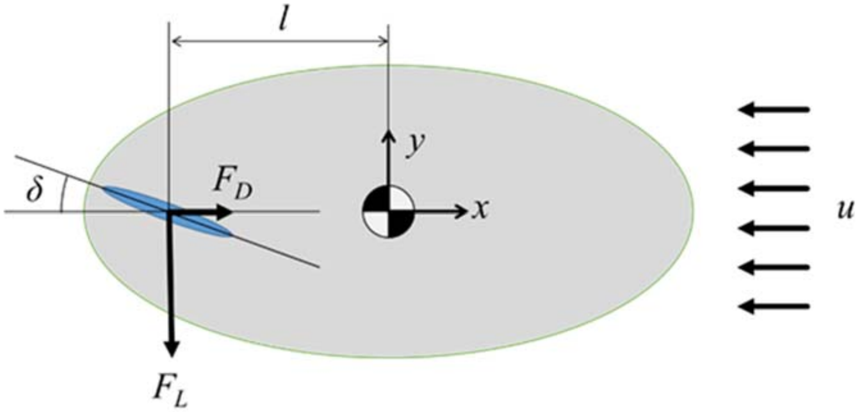

Figure 4-2 Free body diagram of the fin lift force acting on the mUV.

The moments generated by both fins (above and below the mUV) are l distance away form center of mass. The two fins will allow the mUV to yaw and introduces a rotational speed Ω along the z-axis. However, this rotation is not generated unless the vehicle is moving. Therefore, the yaw of the mUV equation can be represented as,

$$I_z \frac{d\Omega}{dt} = -f\Omega + p\delta u|u| \tag{4.7}$$

where I_z is the moment of inertia of the mUV along the z-axis, f is the damping coefficient, and p is the constant $\rho C_L H l$.

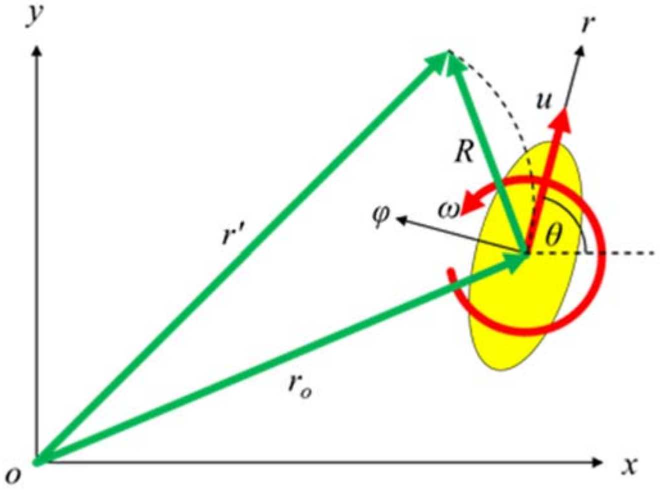

Figure 4-3 The relation between the stationaty reference fram and the moving reference frame of the mUV.

For a vehicle with a local coordinates (*r*,*φ*), moving forward at a velocity *u* and rotating at an angular velocity *ω* generated by fins at a distance *l* form the center of mass of the vehicle.

$$\bar{u} = \begin{bmatrix} u \\ \omega l \end{bmatrix}_{\hat{\varphi},\hat{r}} . \tag{4.8}$$

Assuming an initial velocity V_o and defined as,

$$\overline{V_o} = \begin{bmatrix} V_{ox} \\ V_{oy} \end{bmatrix}_{\hat{i},\hat{j}} . \tag{4.9}$$

The transformation from the local frame to the global frame is,

$$\mathbf{R} = \begin{bmatrix} \cos(\theta) & -\sin(\theta) \\ \sin(\theta) & \cos(\theta) \end{bmatrix} . \tag{4.10}$$

Therefore, the transformation of the mUV velocity $\overline{V}_{r'}$ from the local coordinates to the global coordinates is,

$$\overline{V}_{r'} = \overline{V}_0 + \mathbf{R}\overline{u} \ . \tag{4.11}$$

The vehicle yaw angle θ can be expressed as,

$$\frac{d\varphi}{dt} = \Omega \, . \tag{4.12}$$

Assuming,

$$\overline{V}_{r'} = \begin{bmatrix} \dfrac{dx}{dt} \\ \dfrac{dy}{dt} \end{bmatrix}_{\hat{i},\hat{j}} \ . \tag{4.13}$$

the *x* and *y* position of the mUV are,

$$\frac{dx}{dt} = V_{ox} + u\cos(\theta) - \Omega l \sin(\theta), \tag{4.14}$$

$$\text{and } \frac{dy}{dt} = V_{oy} + u\sin(\theta) + \Omega l \cos(\theta). \tag{4.15}$$

Choosing *u*, *ω*, Ω, θ, *x* and *y* to be state variables (x_1, x_2, x_3, x_4, x_5 and x_6) respectively. In addition, I_{net} and *S* to be the inputs u_1 and u_2. Hence, the state space representation can be rewritten as,

$$\begin{aligned}
\dot{x}_1 &= a_{11}x_2|x_2| - a_{12}x_1|x_1| \\
\dot{x}_2 &= -a_{21}x_2 - a_{22}x_2|x_2| + b_{21}u_1 \\
\dot{x}_3 &= -a_{31}x_3 + b_{31}x_1|x_1|u_2 \\
\dot{x}_4 &= x_3 \\
\dot{x}_5 &= V_{ox} + x_1\cos(x_4) - a_{51}x_3\sin(x_4) \\
\dot{x}_6 &= V_{oy} + x_1\sin(x_4) + a_{51}x_3\cos(x_4)
\end{aligned}\quad, \tag{4.16}$$

$$\left.\begin{aligned}
a_{11} &= \frac{C_T\rho d^4}{m} \\
a_{12} &= \frac{C_D\rho A}{2m} \\
a_{21} &= \frac{b}{J} \\
a_{22} &= \frac{C_Q\rho d^5}{J} \\
a_{31} &= \frac{f}{M} \\
a_{51} &= l \\
b_{21} &= \frac{K_T}{J} \\
b_{31} &= \frac{p}{M}
\end{aligned}\right\}, \tag{4.17}$$

5. BRUSHLESS THREE-PHASE DC MOTOR DESIGN

5.1. Introduction

The motor is the most important component of the mUV. It plays a major role in the propulsion system. However, the size of the motor and its performance must meet the criteria of the mUV. An inrunner three-phase brushless permanent magnets DC motor with Hall Effect sensors was designed to fit inside the mUV's core. The desired dimensions of the motor involve a 3 inch outer diameter and 1.25 inch length. The rotor is designed to fit a long ring propeller 1.625 inches in diameter and 2.625 inches in length. The motor is composed of a stator with nine slots and three pull pair magnets with an air gap thickness of 1.15mm. Two thin-section bearings were used to hold the rotor and allow it to rotate freely (see Figure 5-1).

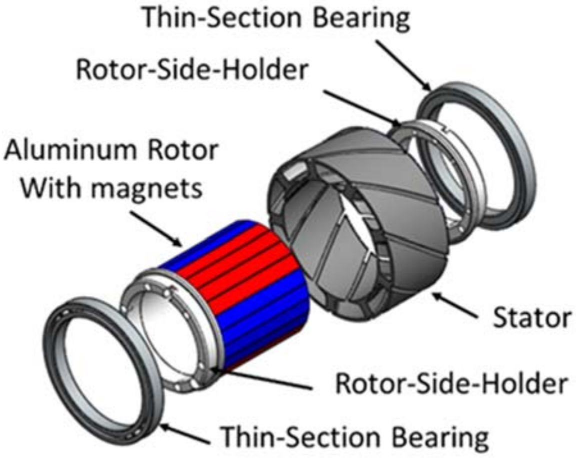

Figure 5-1 Brushless DC motor exploded showing the electric steel stator core stack and aluminum rotor with permanent magnets.

5.2. Stator development

Nine slots brushless DC motor was designed using Solidworks (V.2011, Dassault Systems). A section of the stator with dimensions is shown in Figure 5-2 . A 1.25 inch high stator core was assembled from stacks of electrical steel laminations that have a high relative magnetic permeability (about 4000). The purpose of the lamination stack is to reduce the eddy-current and improve overall motor efficiency (Atallah, 1992; Greig & Sathirakul, 1961). The assembly of the stator core was formed from those electric steel laminations with a skew angle of 20^o to reduce torque cogging and enable smooth motor rotation startup (Islam, 2009; Yeadon, 2001). Skewing complicates numerical electromagnetic analysis. The simulation is usually time consuming since it requires 3-D finite elements analysis (FEA) or 2-D models with many slices (Holik, Dorrell, Lombard, Thougaard, & Jensen, 2006). The stator core was insulated using a specific epoxy stator-insulation material. The custom cuts of the stator laminations were fabricated by Proto Lamination Inc. and assembled by Winding Inc.

Each tooth was winded by hand with 25 clockwise turns in the form of (ABCABCABC) using 22 gauge copper wire to form three-phase stator windings. During the winding, each phase was tested for short circuit using a multimeter. Wye configuration was formed out of the three-phases. In addition, three Hall Effect sensors were placed (with 40^o a part from each other) on to the stator to control the rotation speed of the rotor. The brushless motor speed was controlled using a brushless speed controller (MDC010-050101, Anaheim Automation).

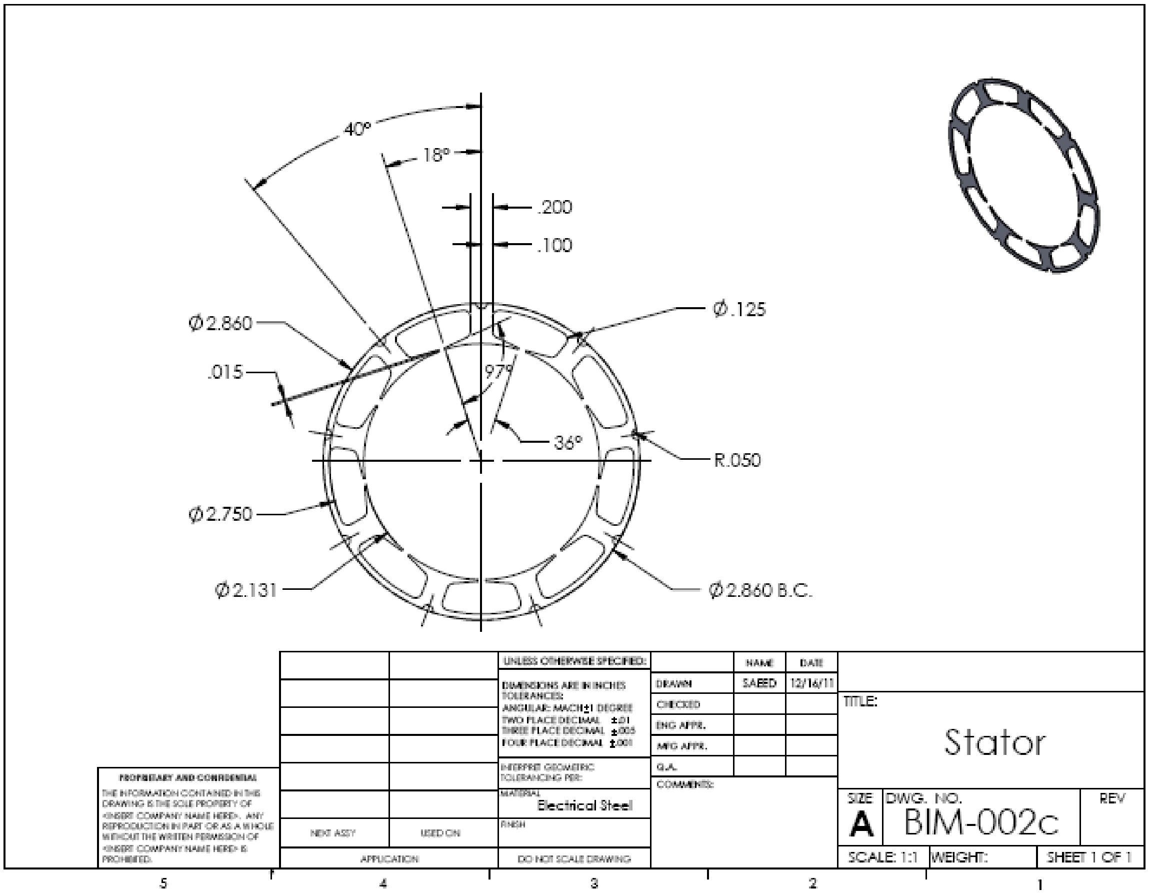

Figure 5-2 A two dimentional drawing for the stator with nine slots using Solidworks.

5.3. Rotor development

The rotor is in the shape of hollow cylinder and is made of aluminum with 24 magnet blocks assembled around it. The aluminum hollow cylinder is 2 inches long with a 1.90-inch outer diameter and a 1.625-inch inner diameter. The outer diameter of the rotor was shaved in the longitude direction evenly and at a width of 1/4 inches. Each magnetic block is 2 inches long, 1/4 inches wide and 1/16 inches thick, which is magnetized through thickness. Each four magnets were put together in the same polarity to form one magnetic pulling force. All magnets were mechanically fixed to the aluminum cylindrical rotor using two aluminum rotor-side-holders on each side.

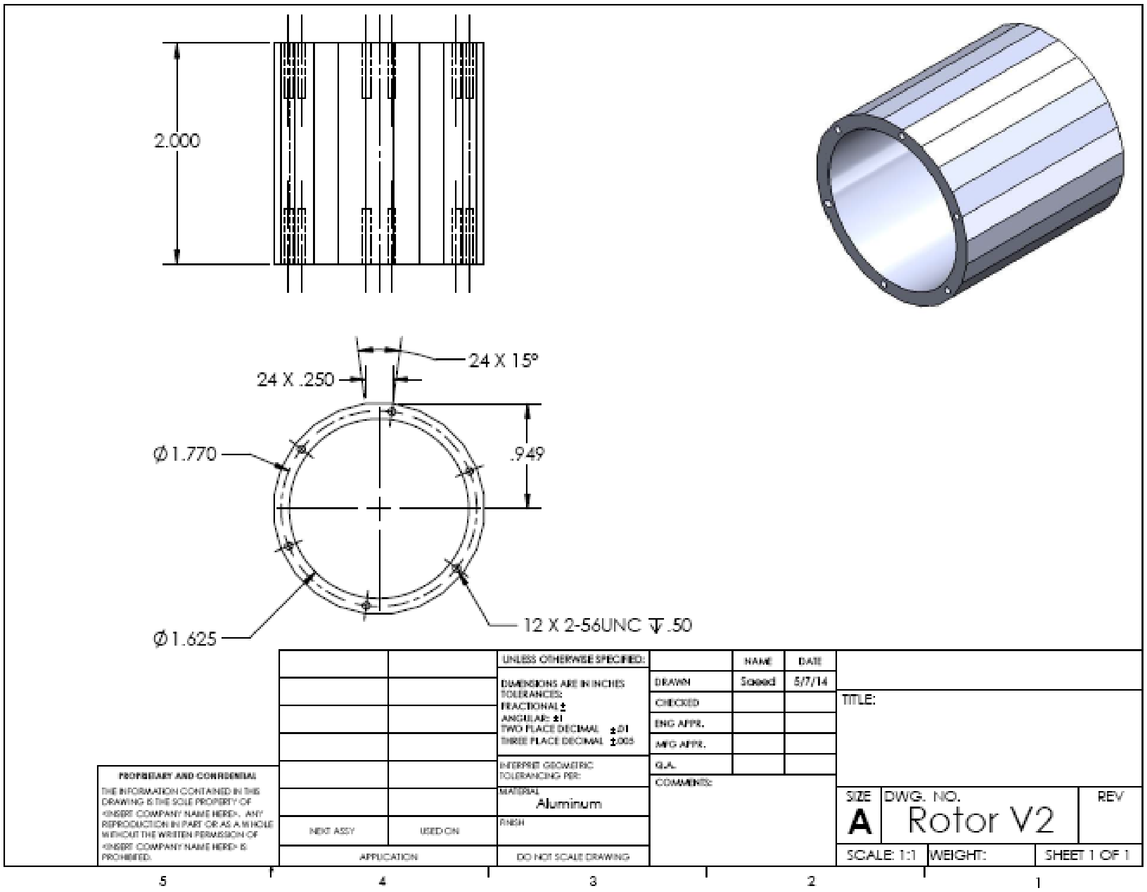

Figure 5-3 A two dimentional drawing for the rotor with 24 flat surfaces around the outer diameter using Solidworks.

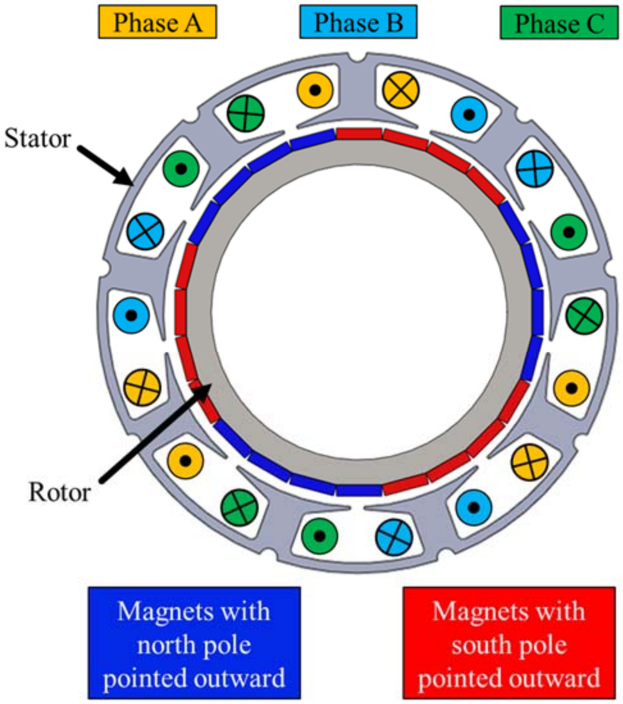

Figure 5-4 Schematics of the three-phase brushless DC motor with stator winding and rotor magnets.

5.4. Rotor side-holders design

The magnets were put together around the aluminum rotor and mechanically fixed using two rotor-side-holders. Figure 5-5 shows the two dimensional drawing for the rotor-side holder-part using Solidworks. The two side-holders are assembled with the rotor and the magnets using 2-56 size screws to form the rotor magnets of the motor. The rotor is held by two commercially available thing-section-bearing through each rotor-side-holder.

Figure 5-6 shows the anatomy of the brushless motor. It also shows the actual brushless motor after the assembly. Side-motor-housings were machined to hold the stator and the thin-section-bearing together for motor testing purposes.

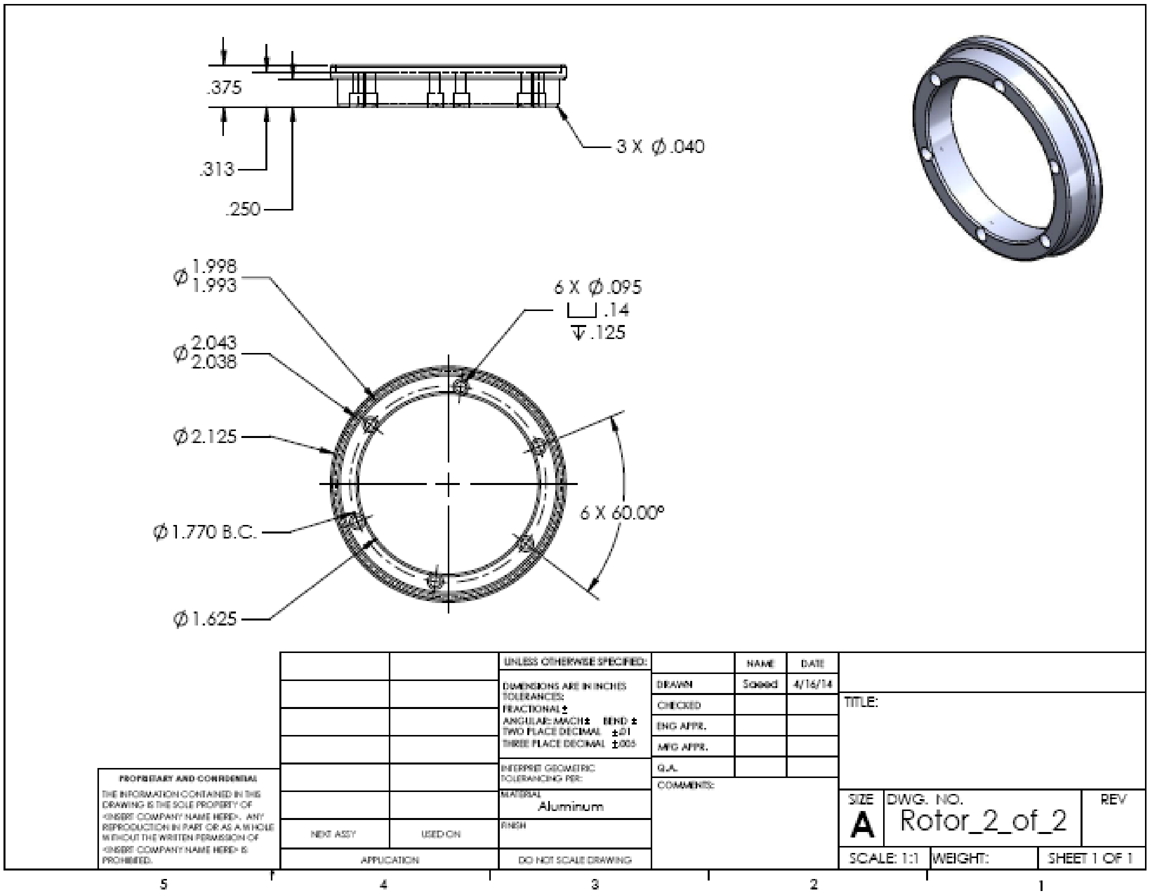

Figure 5-5 A two dimentional drawing for the rotor-side-holders using Solidworks.

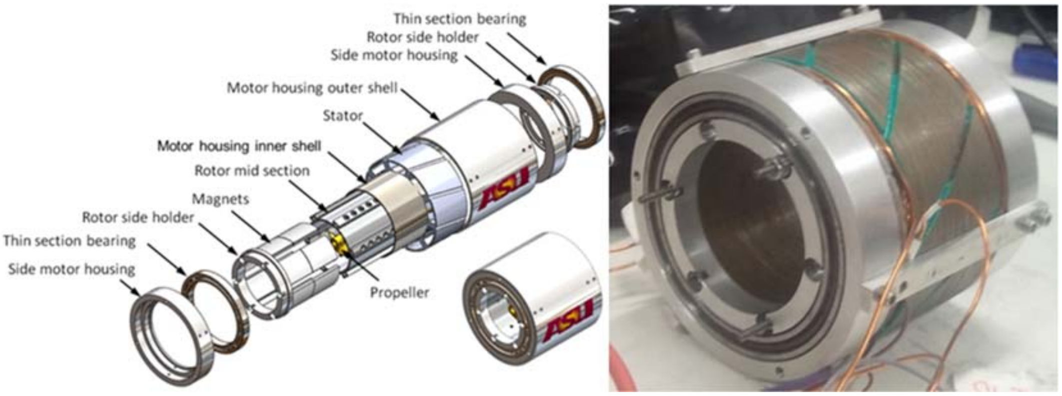

Figure 5-6 The anatomy of the motor-thruster components exploded.

5.5. Motor numerical simulation

The motor cross-section was simulated in two-dimensional COMSOL Multiphysics simulation package. The assumption of skewing was neglected and the stator core and rotor core without losses. The model was simulated with the Rotating Machinery and Magnetic (*rmm*). A constant rotor speed (1000 RPM) was applied to the rotor to study the corresponding generated back EMF. The simulation computed the flux distribution and the magnetic flux density are shown in Figure 5-7. In addition, the back EMF as a function of rotor position is plotted in Figure 5-8. The motor voltage constant was calculated to be 0.015 V.s/rad.

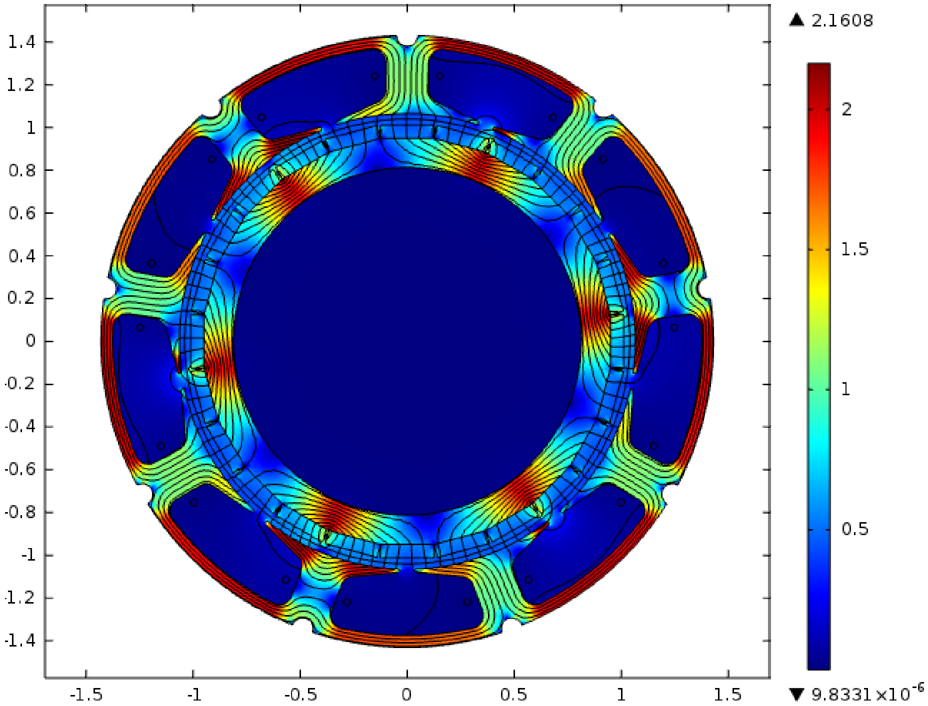

Figure 5-7 2D FEA model showing flux distribution and magnetic flux density in Tesla with no-load at a spicific rotor position.

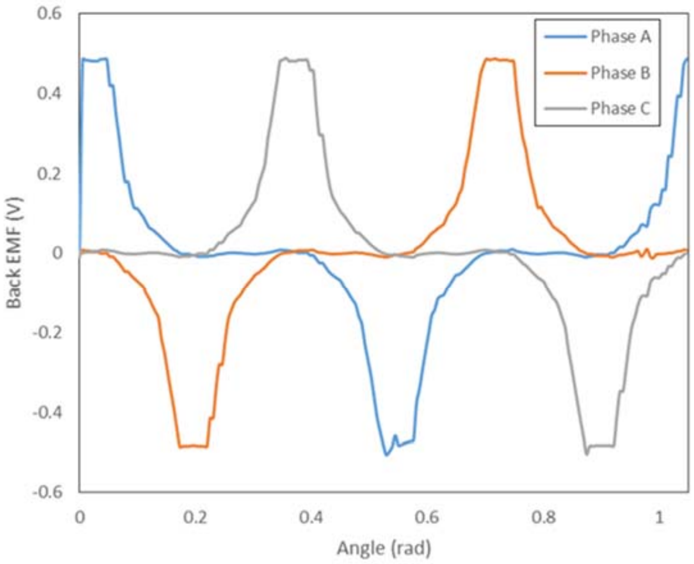

Figure 5-8 Motor back EMF ploted as a function of the rotor position simulated by COMSOL Multiphysics.

5.6. Damping coefficient of the thin-section-bearings

The damping coefficient can be estimated using the equation of motion equation (4.1) for the brushless DC motor. Since there is no propeller or actual load, the torque resistance is zero. In addition, without the brushless DC motor, the input electric current variable is zero as well. The ODE becomes $\dot{\omega} = -\frac{b}{J}\omega$ and it can be solved which represent an exponential decay equation.

$$\omega(t) = \omega(0)e^{-\frac{b}{J}t} \tag{5.1}$$

The rotational speed can be described as a function of time curve as a line such that the slope *m* is the derivative of *ω*(*t*) at time zero and the *y*-intercept as the initial rotational speed $\omega(0)$. However, in order to get good linear regression fit to the curve, a high value for the moment of inertia (i.e. high time constant) must be chosen.

$$b \approx -\frac{mJ}{\omega(0)} \tag{5.2}$$

The experiment was performed using a flywheel held by the bearings on both sides. The rotational speed was measured using a Photodiode which measure the frequency of light intensity passing through the checkerboard aligned at the boundary of the wheel (see Figure 5-9).

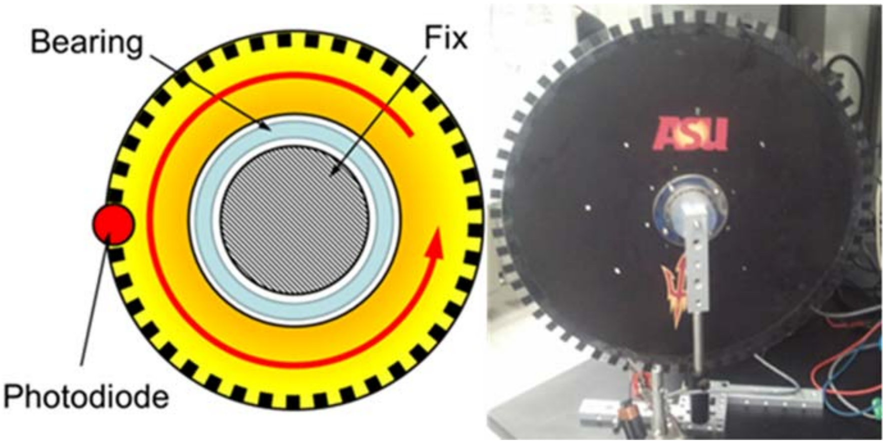

Figure 5-9 Schematic and experiment setup for the flywheel with bearing attached to the sides and optical sensor to measure the speed of the wheel using LabVIEW.

A LabVIEW user interface was developed to generate the data. This data was analyzed which shows a damping coefficient of $1.42 \times 10^{-4} \pm 0.0965 \times 10^{-4}$ with 95.4% certainty (see Figure 5-10).

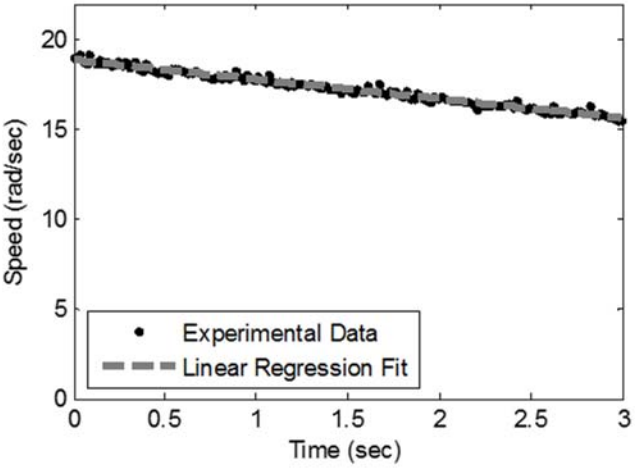

Figure 5-10 One of the experimental data of the flywheel rotational speed vs. time.

5.7. Motor torque constant experiment

The brushless motor with Hall-Effect sensors and a speed controller were assembled and put through testing to measure its torque constant K_T. A 0.05 ohms shunt resistor (MP930-0.050-1%, CADDOCK) was added in series between the power supply (30 V) and the motor controller in order to measure the input DC current flowing through by measuring the potential voltage drop around it using a National Instrument Data Acquisition (DAQ) card (6035E, National Instruments) . In parallel, the rotor position θ as a function of time was measured by recording the potential drop across one of the Hall-Effect sensors using the same DAQ card. A schematic of the experiment setup is shown in Figure 5-11. Using LabVIEW (Version 8.6, National Instruments), the signals were recorded for different reference speed inputs (Speed Knob). The measured DC current, I_{net}, was plotted as a function of the rotor rotational speed ω.

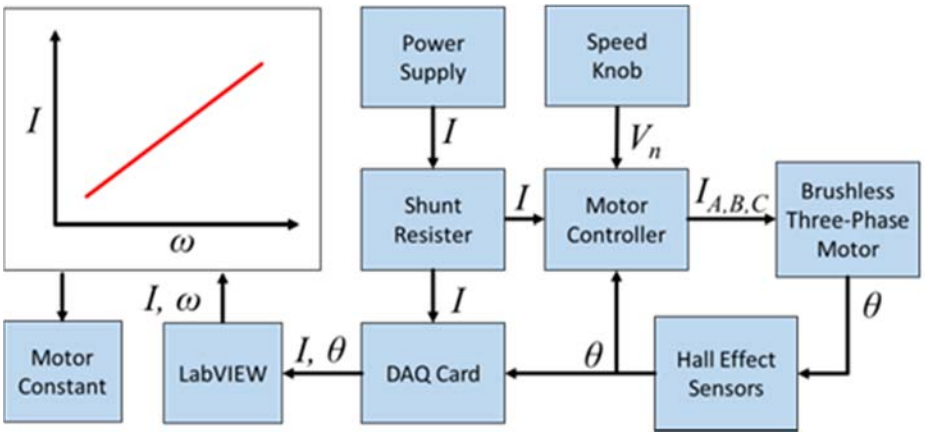

Figure 5-11 Block diagram to show the process and the connection of the motor to measure the motor torque constant.

The current was measured using an ammeter and the rotational speed was measured using Hall Effect sensors (see Figure 5-12).

In a steady state with no torque load, equation (4.1) can be simplified as,

$$\omega = \frac{K_T}{b} I_{net} \tag{5.3}$$

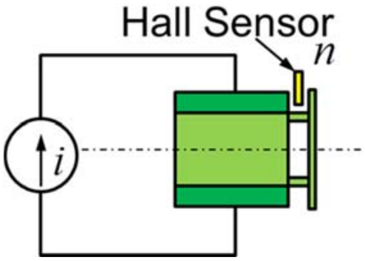

Figure 5-12 Schematic to show the experimental setup of the motor to measure the motor toque constant (KT) through the input electric current (I) and the rotor speed (ω).

The experiment was performed and the rotor rotational speed *ω* was measured against the input electrical rated current I_{net}. The motor torque constant was calculated from the slope to be 0.014 N.m/A (see Figure 5-13). This value was obtained after performing a small experiment to determine the damping coefficient of the thin-section bearings *b*.

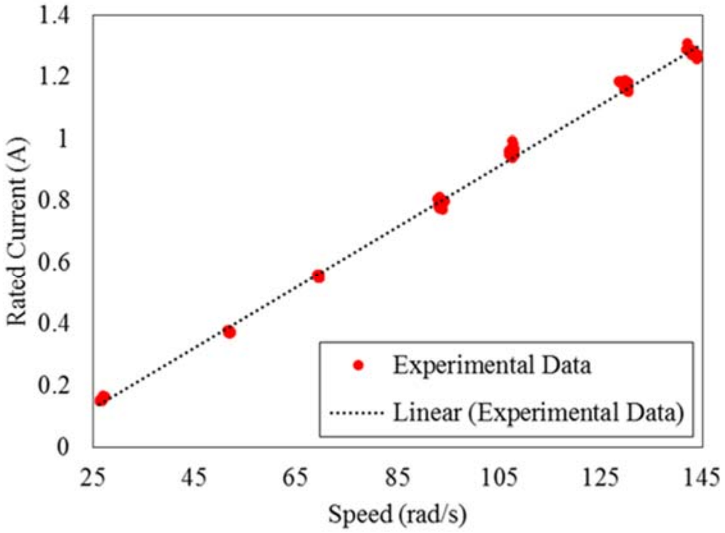

Figure 5-13 One of the experimental data of the motor speed vs. electric current with a linear regression fit.

5.8. Discussion and conclusion

The three-phase brushless DC motor with permanent magnets was designed and fabricated to become part of the propulsion system of the miniaturized underwater vehicle. The most critical part of this design was the stator and the stator winding. The winding process was not only time consuming but also critical. The copper wire required to be winded without necking or bleeding the wire insulation. After each tooth winding, the wire were inspected to short circuit. After each phase winding, the resistance and the inductance were measured and confirmed to match the other phases.

The motor torque constant was determined numerically and experimentally to be about 0.014. The measured data suggested a linear relationship between the rotor speed and the input electric current. The torque constant can be improved by modifying the stator structure. It can also be improved by increasing the number of wire turns through each stator tooth. However, the winding was done by hand which permit room for error and uneven distributions throughout the stator. Plan is to use machines to wind the stator, which not only give a homogenous distribution, but also allows increasing the number or turns.

6. VEHICLE INSULATION PRESSURE HOUSING DESIGN

6.1. Introduction

Many long traveling range underwater vehicles have a torpedo shaped vessel. This shape improves the aerodynamics and motion energy required for the underwater vehicle (Davis, Eriksen, & Jones, 2002). Our proposed torpedo shaped can be described as three assembly segments. The first segment is the frontal area. This segment is considered the hotel load segment where all the underwater sensors and measurement devices can be carried by the underwater vehicle. The second segment is the middle part with a hollow cylinder shape. This segment is the most critical part since it has the propulsion system and all electronics components stored inside the cylinder. The third segment is dedicated for the navigation system. It also includes the fins and necessary modules to enable the mUV with the capability of turning.

6.2. New pressure housing design technique

A method is proposed to design an underwater thruster with a pressure-housing insulator specifically applied to an inrunner three-phase brushless DC motor stator winding. The pressure-housing wall is situated through the air gap between the stator and the rotor magnets (see Figure 6-1). The wall thickness of the pressure housing must be thinner than the air gap between the rotor and stator. In addition, a ring thruster is attached directly to the hollow, cylindrically shaped rotor magnets.

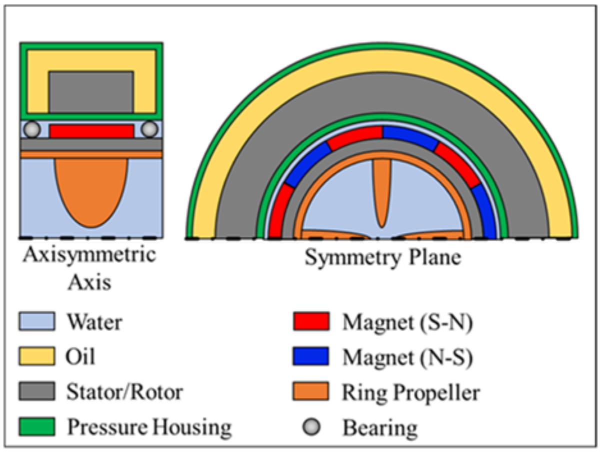

Figure 6-1 A schematic of the proposed method to insulate propulsion system.

This new configuration was inspired by the current methods of deep-sea underwater housing designs. Figure 6-2 shows the most common types of oil-filled pressure housing. A motor can be encapsulated inside an oil-filled pressure-housing unit with a rotor shaft sticking out through a radial shaft seal (Figure 6-2A). A shaft seal usually is composed of an auxiliary lip that protects the primary sealing lip from leaking oil out or leaking seawater in (Sasdelli, 1971). This type of seal may not be practical in high-pressure environments such as the deep-sea (Tonder, 1992). However, it can work with the existence of pressure balancing modules (Allen, 1997). In addition, this type of pressure housing and sealing become more challenging and expensive as the water depth increases (Jahnke, 1989). Figure 6-2B is another type of pressure housing design; however, it does not require a shaft seal. The rotor shaft remains inside the pressure housing. The motion is transmitted through the pressure-housing wall by a magnetic coupling drive. This concept works by aligning opposite magnetic poles to generate attraction and repulsion forces between two hubs, causing several magnetic poles to transmit torque from one magnet hub to the other. The disadvantage of this type of coupling is that without careful alignment, vibrations will be present which cause power transmission reductions and poor efficiency (Post, 1999).

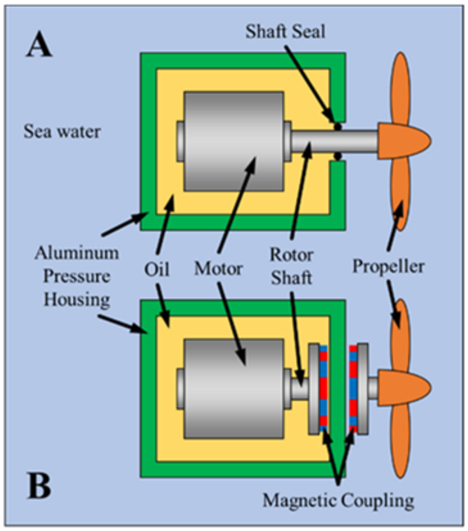

Figure 6-2 Oil-filled pressure housing unit to protect electronic components by preventing corrosion and avoiding short circuits. (A) Housing design with shaft seal. (B) Housing with a magnetic coupling drive.

The propulsion system must be insulated and filled with syntactic foam and oil to prevent the system electronics from the ocean water as it can short out the circuit due to the high conductivity in the salty water. In addition, the housing material of this segment must be compatible with the deep-sea environment to prevent material failure such as cracking and corrosion. Syntactic foam is a composite material of epoxy and ceramics. It is known for its strength and low density, which ideal for deep-sea application. This material often used to balance the overall vehicle specific density and drive it to naturally buoyant.

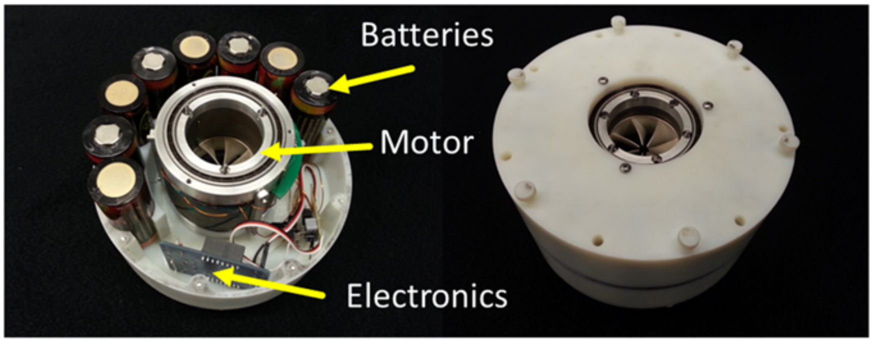

Figure 6-3 Propulsion system insice an oil filling pressure resistance housing prototyp.

For underwater motor testing, a plastic (Vero white) housing was three-dimensional printed (see Figure 6-4). This housing can insulate the entire stator winding and prevent the electronics from getting wet.

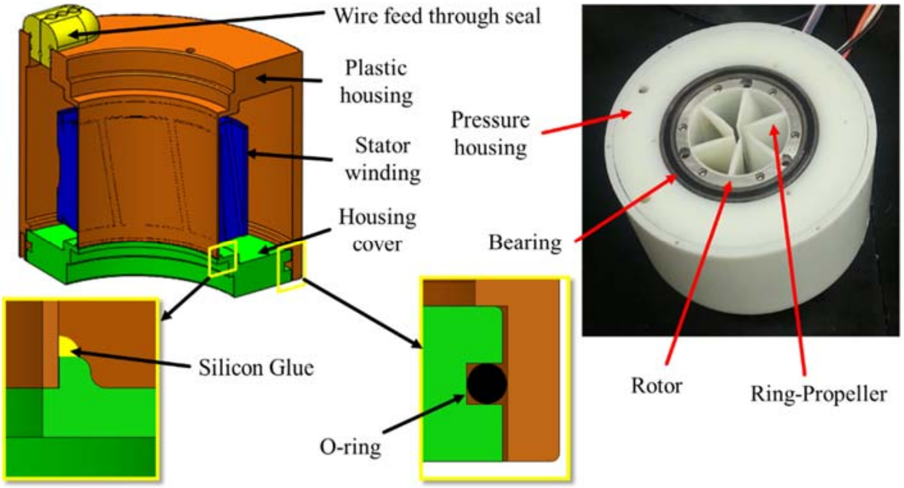

Figure 6-4 Plastic housing 3-D printed to insulate the stator winding from getting wet.

6.3. Deep-sea propulsion system pressure housing

In order to have a compatible deep-sea vehicle, certain criteria must be met. The most important factor is pressure resistance. The deep ocean environment has high pressures, which vary and depend on the depth from sea levels. For example at 3000 m depth, the pressure can get as high as 6000 psi. The middle section, (i.e. the propulsion system) is considered one of the critical sections due to sensitivity of its contents to high pressures and water salinity. The propulsion system is composed of a brushless DC motor, bearings, a propeller, batteries, electronic circuit boards and connecting wires. All of the propulsion systems except the propeller, bearings, and rotor magnets must be protected from high pressure and ocean water. Therefore, a pressure resistance oil filled housing is necessary to prevent the propulsion system components from malfunctioning.

To design such housing, certain steps are necessary to be followed.

- Design the CAD model of the deep-sea housing (Pressure vessel). Figure 6-5 proposes the pressure resistance housing structure.
- Select a deep-sea compatible material to fabricate the housing with, such as an aluminum alloy 5086.
- Perform a FEA simulation to determine the failure points. See Figure 6-6.
- Iterate the design and re-simulate the FEA model with the new geometry to ensure no failure mode acquire.
- Enable traditional deep-sea surface treatment of the aluminum alloy by anodizing, TUFRAMR, electrolysis nickel plating, electroless nickel-plating, and painting.

TUFRAMR is a technique to make a surface enhancing coating of General Magnaplate.

- Assemble the propulsion system and integrate into the housing.
- Fill with oil and syntactic foam to balance buoyancy in the water.
- Seal the housing.
- Test propulsion system inside a deep ocean simulator. Pressure testing facility in San Diego (www.deepsea.com) is the ideal place for this test.
- Iterate the design and repeat the process again until satisfactory results are achieved.

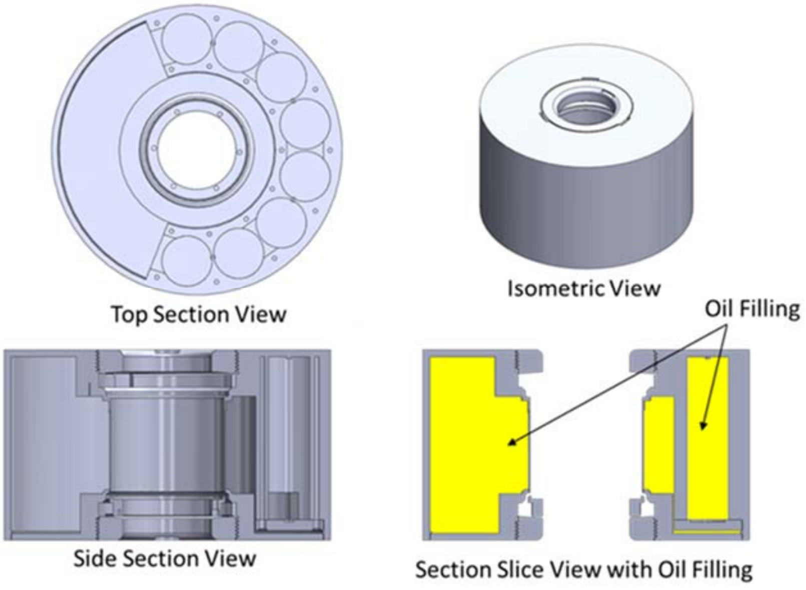

Figure 6-5 Pressure resistance housing CAD model.

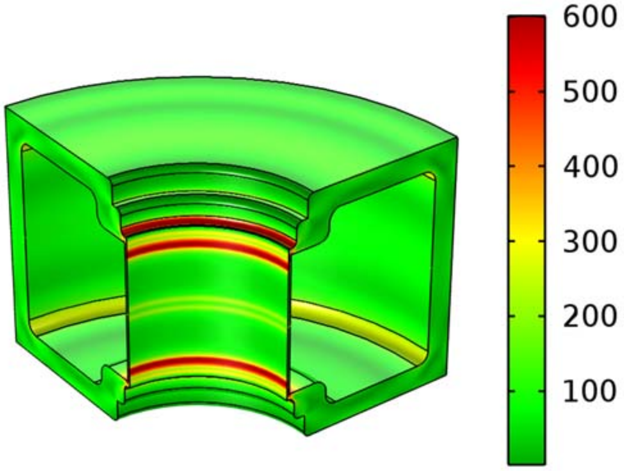

Figure 6-6 FEA of the pressure resistance housing simulated with COMSOL Multiphysics showing Von Mises. Stress in MPa

6.4. Discussion and conclusion

Ideally, a propulsion system must be insulated and filled with non-conductive fluid composing of a specific density lower than one, in order to achieve natural buoyancy. In addition, the pressure housing material must be compatible with the sea environment in order to prevent corrosion. However, in shallow water the environmental pressure is insignificant, leaving the purpose of the housing to ensuring circuit functionality. In contrast, the ambient pressure in the deep-sea environment is usually high. Therefore, the pressure housing must be made of a strong, non-corrosive material such as aluminum alloy 5086 with a minimum required wall thickness. The proposed pressure housing method is simple. The housing wall thickness can be modified to prevent failure. However, with this method, the wall thickness through the air gap is limited. The cylindrically shaped stator can become a support for the thin housing wall, which prevents it from deflection. The deep-sea pressure housing using this method will be designed and analyzed in future work and it will not be discussed in this paper.

For underwater motor testing, the pressure housing was three-dimensionally printed using a plastic material (VeroWhite). The housing is composed of the main body as well as a cover; the cover seals the housing using a silicon glue and an O-ring. This specific housing was tested and is capable of insulating the entire stator winding in order to prevent water interference with the electronics.

7. PROPELLER OPTIMIZATION

7.1. Introduction

Underwater vehicle thrusters have a major impact on the vehicle system dynamic. The size, shape, and speed of any propeller dominate the overall performance in terms of trust and torque generated. (Manwel, McGowan, & Rogers, 2002) The shape of the blade cross-section and its orientation dictate the efficiency of the propeller. For a traditional propeller with an almost flat plate shaped blade cross-section, the lift and drag forces can be shown in the free body diagram (FBD) in Figure 7-1. The airfoil rotating about the axis of rotation at an angle $\theta - \alpha$ generates a lift and drag forces (dF_L and dF_D). The vertical velocity of the airfoil can be described as the product of the propeller rotational speed ω and the radial distance r between the airfoil section and the center of the propeller. The horizontal velocity of the propeller is denoted as u.

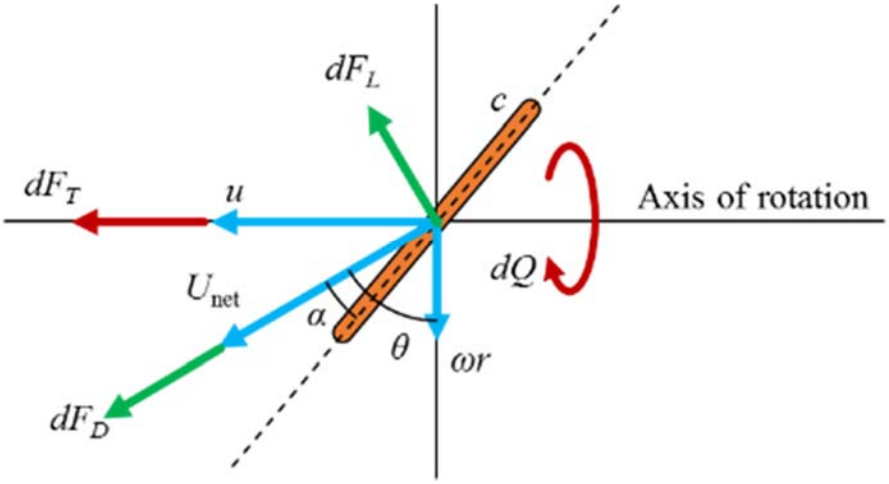

Figure 7-1 Free Body Diagram (FBD) of an airfoil (flat plate with a chord length c) rotating about the axis of rotation with a speed ω.

Therefore, the thrust and torque generated by the propeller is as following,

$$dF_T = B\frac{1}{2}\rho U_{net}^2\left[C_L\cos(\theta) + C_D\sin(\theta)\right]cdr \tag{7.1}$$

$$dQ = B\frac{1}{2}\rho U_{net}^2\left[C_L\sin(\theta) - C_D\cos(\theta)\right]crdr \tag{7.2}$$

$$U_{net}^2 = u^2 + \omega^2 r^2 \tag{7.3}$$

where B is the number of blades and U_{net} is the overall speed of the propeller assuming no slip is generated.

7.2. Numerical simulation

The coefficients C_L and C_D depend on the Reynolds Number (Re) and the angle of attack. The best performance of the propeller can be achieved by maximizing the lift over drag coefficient ratios. A thin elliptical shape (almost flat) was chosen to benefit from the symmetry and to allow the propeller to perform similarly if it rotates clockwise or counter clockwise. Using COMSOL Muliphysics, the ellipse was simulated by exposing it to a horizontal flow. Two parameter factors values, Reynolds Number Re and angle of attack α were changed to determine the best performance of the airfoil. Figure 7-2 shows a representative scaled velocity field of the fluid passing through the airfoil.

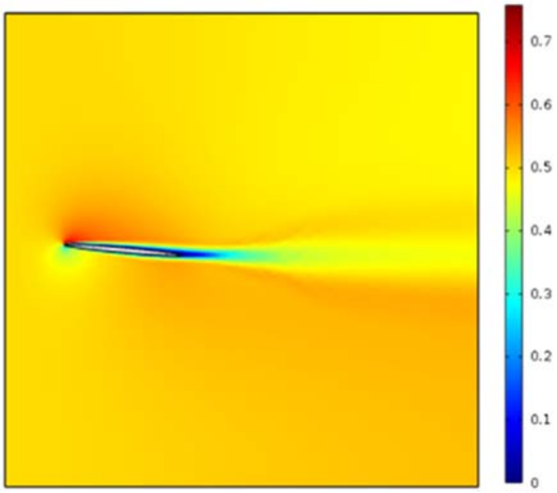

Figure 7-2 A representative scaled velocity field results of COMSOL Muliphysics simulation of the ellipse at Re = 100000 and α = 5º.

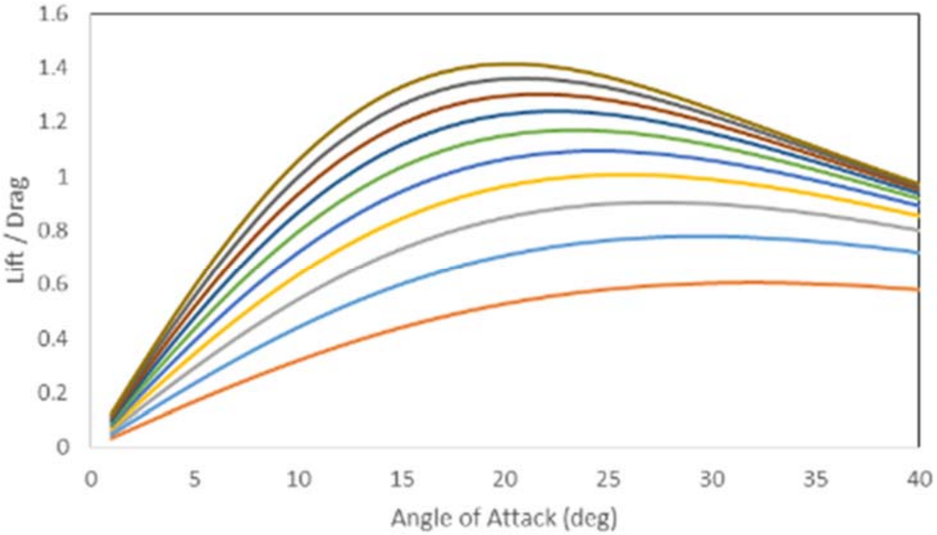

Figure 7-3 Lift over drag ratio of the airfoil for Re range of 5000 (lowest curve) to 50000 (heighest curve) at 5000 steps.

7.3. CAD model design

Several CAD model propellers were created with different twist angles and blades number then three dimensionally printed using 3D printer (see Figure 7-4). Sixteen propellers with combinations of (4, 5, 6, and 7) blades and (60, 80, 100, and 120) degrees were made. Another set of four propellers were made with extended three and four blades with 40° and 60° twist angles (see Figure 7-4) which should perform better aerodynamically. Each propeller was tested underwater with different speeds. The results are going to be shown in the Experiments and Results, Thrust and Torque coefficient section.

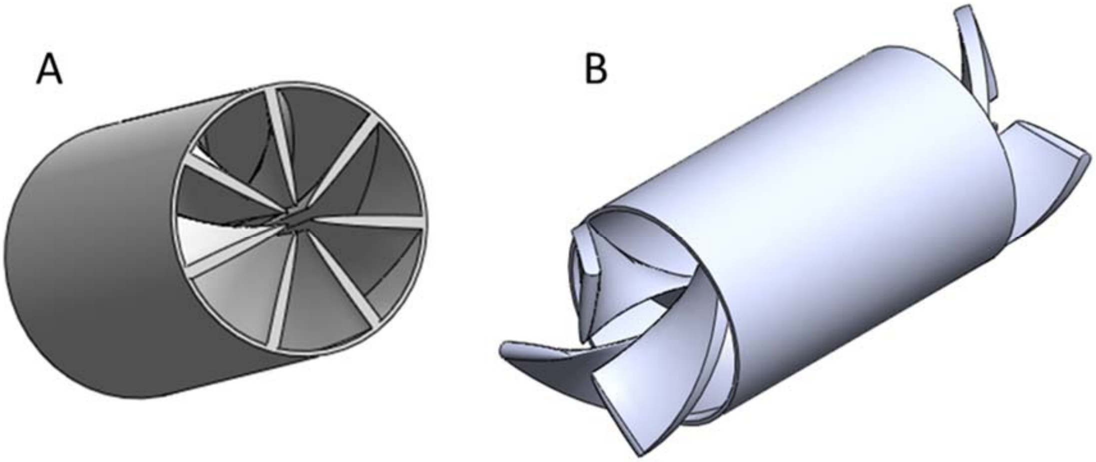

Figure 7-4 CAD drawing for (A) Ring-thruster with seven blades and 100° twist angle. (B) Ring-thruster with three extended blads and 60° twist angle.

7.4. Experimental setup

Figure 7-5 shows the schematics of the experimental setup for both cases of thrust and torque measurements. The structure stand was constructed from T-Slots beams

(47065T101, McMaster-Carr) to hold the motor in both configurations (thrust and torque). This method was adopted from (Healey et al, 1995).

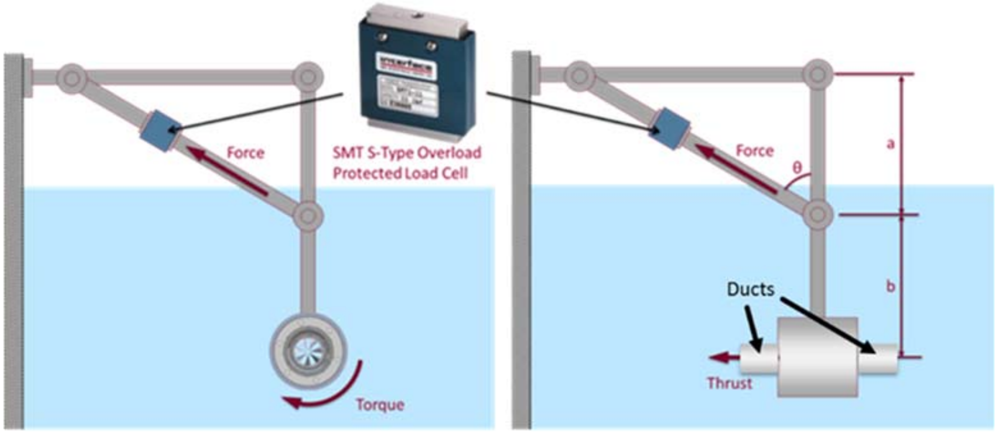

Figure 7-5 Schematics of the experimental setup to measure thrust and torque as function of ring thruster speed.

Using structural mechanics, I can determine the relationship between the thrust (or torque) and the compression or the tension force in the sensor.

$$F_T = \frac{a\sin(\theta)}{a+b} F_S \tag{7.4}$$

$$Q = a\sin(\theta) F_S \tag{7.5}$$

where F_S is the force measured by the load cell.

The trust and torque constants (C_T and C_Q) of the ring-propeller can be measured using equations (4.3) and (4.4). Therefore, the propeller speed, thrust and torque measurement are needed to estimate the C_T and C_Q values.

A LabVIEW code was generated to interface with the motor speed, motor current and the force sensor (see Figure 7-6).

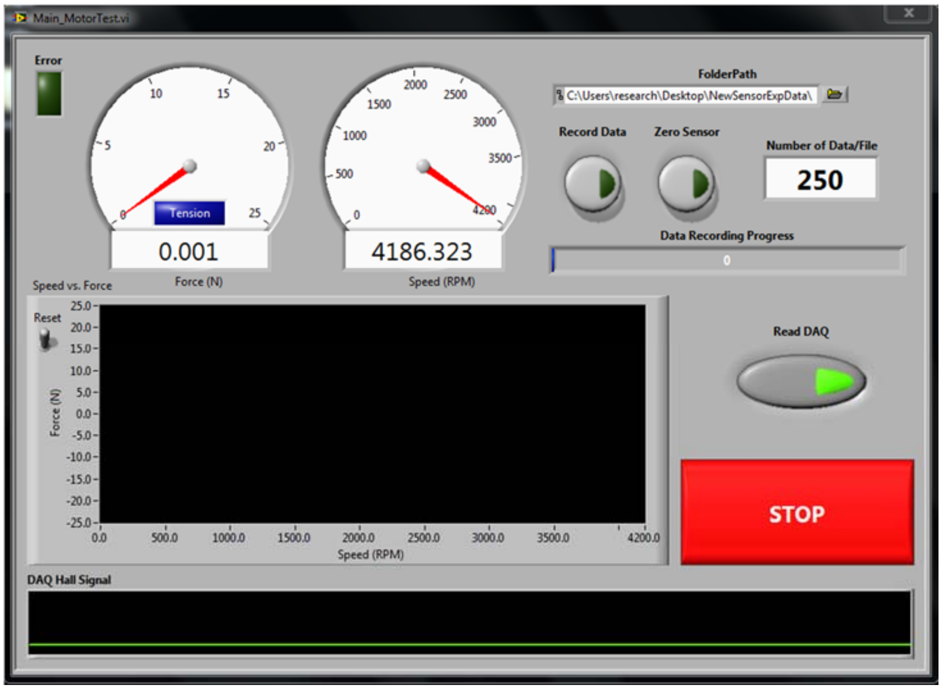

Main_MotorTest.vi

FolderPath: C:\Users\research\Desktop\NewSensorExpData\

Number of Data/File: 250

Force (N): 0.001

Speed (RPM): 4186.323

Figure 7-6 Labview front panal to measure the motor speed, the motor current and the force sensor.

The efficiency of the motor was calculated as the ratio of the torque power output and the electric power input. Similarly, the efficiency of the propulsion system was calculated as the ratio of the thrust power output and the electric power input. The torque power output is the product of the rotor speed and the torque load. The thrust power output is the product of the theoretical advancing speed of the propeller and the thrust generated. The electric power input is the product of the voltage supply value and the input electric current.

7.5. Results and discussion

The experiment was completed to determine the performance of the propulsion system. The brushless DC motor was insulated using the 3D printed housing and sealed properly to ensure no water leakage into the pressure housing. The ring-propellers were tested to measure input electric current, rotor speed, thrust and torque. The thrust F_T was plotted against the quantity ω^2. Sixteen propeller with different blades number and twist angles were tested in water. The thrust and torque of each propeller was measured. Figure 7-7 and Figure 7-8 show the measured thrust vs. the measure propeller speed squared for some propellers. Figure 7-9 shows the measured torque vs. the propeller measured propeller speed squared for one of the extended blades propellers.

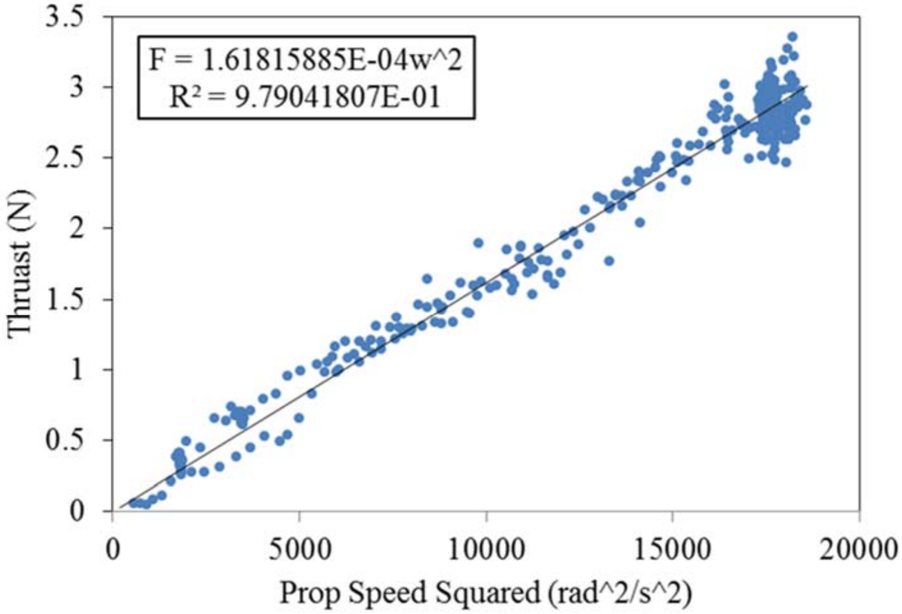

Figure 7-7 Thrust experiemtnal resuts of a non-extended ring thruster with 5 blades and 120^o twist angle.

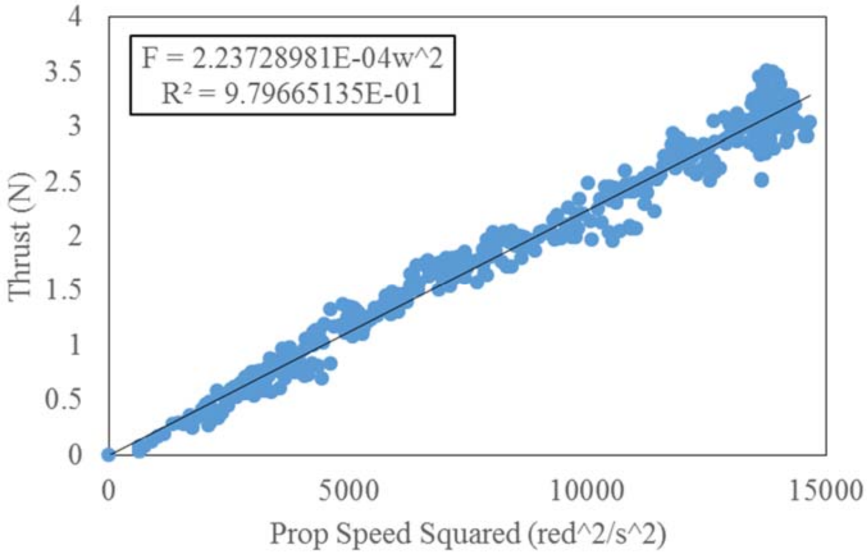

Figure 7-8 Therust experiemtnal resuts of an extended ring thruster with 4 blades and 60^o twist angle.

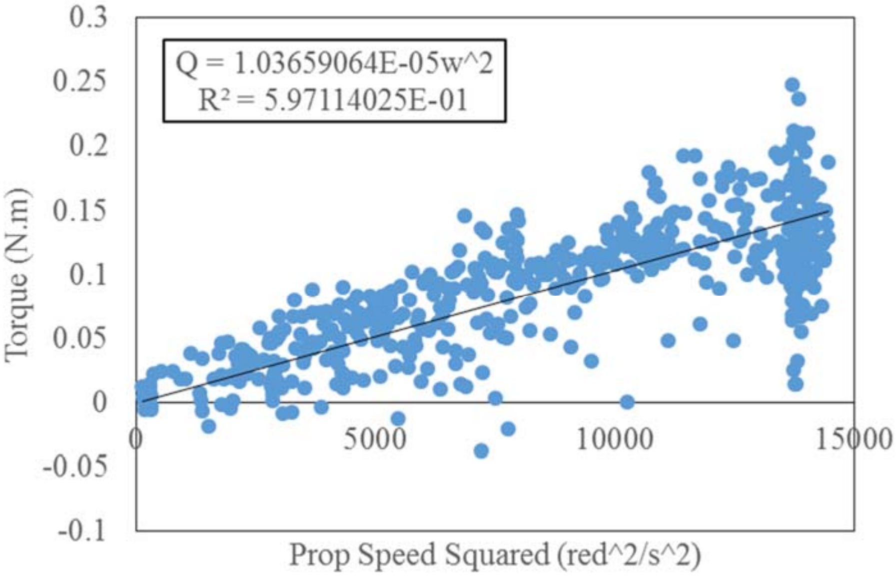

Figure 7-9 Torque experiemtnal resuts of an extended ring thruster with 4 blades and 60^o twist angle.

Figure 7-10 shows a linear relationship between the thrust and $\rho\omega^2 d^4$. The slope represents the thrust coefficient C_T of the ring-propeller, which was approximated to be 0.078 (when the propeller speed measured in rad/s) or 3.08 (when the propeller speed measured in rps).

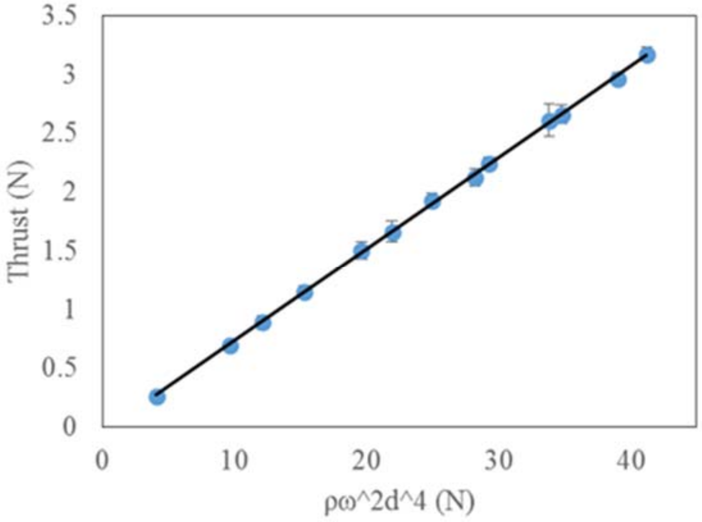

Figure 7-10 Experimental results of the thrust generated by the propeller plotted as a function of the quantity $\rho\omega^2 d^4$.

The input power of the propulsion system can be calculated as the product of the voltage supply (30V) and the measured input electric current. Figure 7-11 shows the measured thrust as a function of the input power. The efficiency of the propulsion system was computed to be about 15.8%.

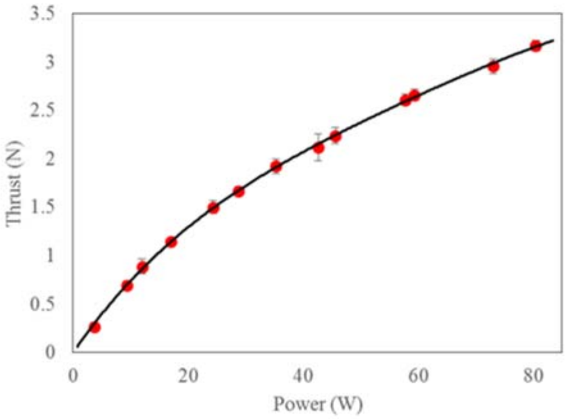

Figure 7-11 Experimental results of the propulsion system thrust as a function of the input power.

Figure 7-12 is the experimental results of the ring-propeller torque plotted as a function of the quantity $\rho\omega^2 d^5$. The relationship between the two quantities should be linear. However, the measured torque was low and associated with a lot of vibrations and disturbance. The disturbance was due to the water movement against the structured stand. The torque constant was approximated to be 0.098 (when the propeller speed measured in rad/s) or 3.86 (when the propeller speed measured in rps). Figure 7-13 shows the measured torque as a function of the input power. The efficiency of the motor at the operating point is 46.84% which conclude that the ring propeller efficiency to be 33.71%.

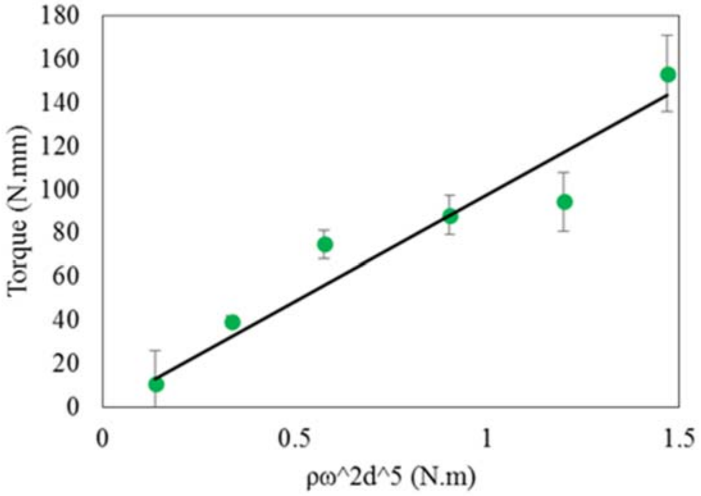

Figure 7-12 Experimental results of the ring-propeller torque as a function of the quantity $\rho\omega^2 d^5$.

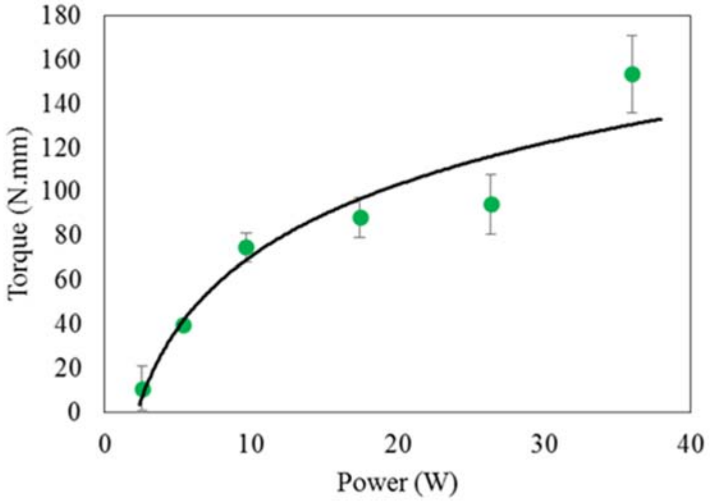

Figure 7-13 Experimental results of the propulsion system Torque as a function of the input power.

8. CONTROLLER DESIGN

Two systems require controller designs. First, the propulsion system that runs by the three-phase DC brushless motor. Second, mUV motion system, which represents the aerodynamics of the vehicle.

8.1. Motor controller

The three-phase DC brushless motor requires an electronics speed controller (ESC). The system (the motor) has three electric currents as inputs and rotor rotational speed as an output. The position sensors can detect the rotor speed as a feedback to the closed loop (see Figure 8-1)

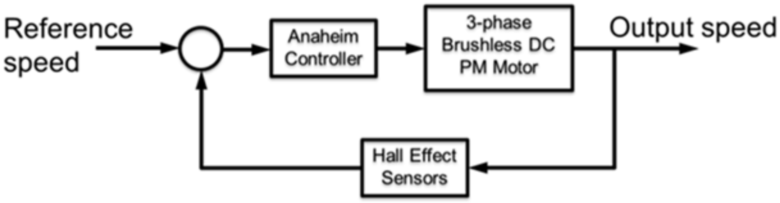

Figure 8-1 Block diagram of the motor system showing a negative feedback control.

Hall Effect sensor where used to measure the rotor speed as a negative feedback to close the loop of the motor using a commercially available controller. The Anaheim Controller (Electrical Commutator, Figure 8-2) produces the necessary electrical currents to rotate the motor at a desired speed.

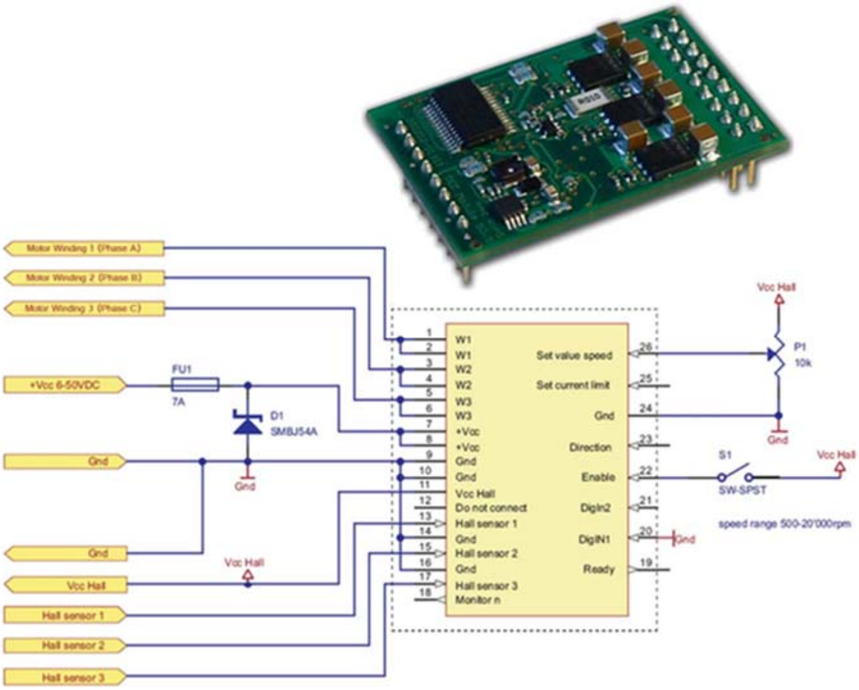

Figure 8-2 Anaheim Automation Brushless Speed Controller board mount with connection diagram.

8.2. Vehicle controller stability

The motor is controlled by the Anaheim controller with a negative closed loop feedback. This subsystem is stable and operates independently. Therefore, the ODE equation (4.16) can be reduced by eliminating x_2 and converted it to an input ($u_3 = x_2|x_2|$) to the new system as it shown in equation (8.1).

$$
\begin{aligned}
\dot{x}_1 &= -a_{12}x_1|x_1| + a_{11}u_3 \\
\dot{x}_3 &= -a_{31}x_3 + b_{31}x_1|x_1|u_2 \\
\dot{x}_4 &= x_3 \\
\dot{x}_5 &= V_{ox} + x_1\cos(x_4) - a_{51}x_3\sin(x_4) \\
\dot{x}_6 &= x_1\sin(x_4) + a_{51}x_3\cos(x_4)
\end{aligned}
\tag{8.1}
$$

Similar concept can be applied to the mUV velocity (x_1) and the mUV yaw speed (x_3). Lyapunov stability analysis was performed on this nonlinear dynamic subsystem with zero inputs. Choosing $V(x)$ to be $1/2\left(x_1^2 + x_3^2\right)$, the $\dot{V}$ (x) can be described as $\dot{V} = -a_{12}x_1^2\left|x_1\right| - a_{31}x_3^2 < 0$ which is always negative for nonzero x_1 and x_3 because the constants coefficients are physical positive values.

8.3. Electric circuit and communications

The propulsion generator has several sub-components such as motor-thruster, motor-controller, and motherboard, PWM-DC converter, batteries and receiver (see Figure 8-3). The motherboard circuit (PCB) was designed with Eagle CAD software (Figure 8-4) to interface with the motor, motor controller, PWM-DC converters, receiver and battery back (see Figure 8-5).

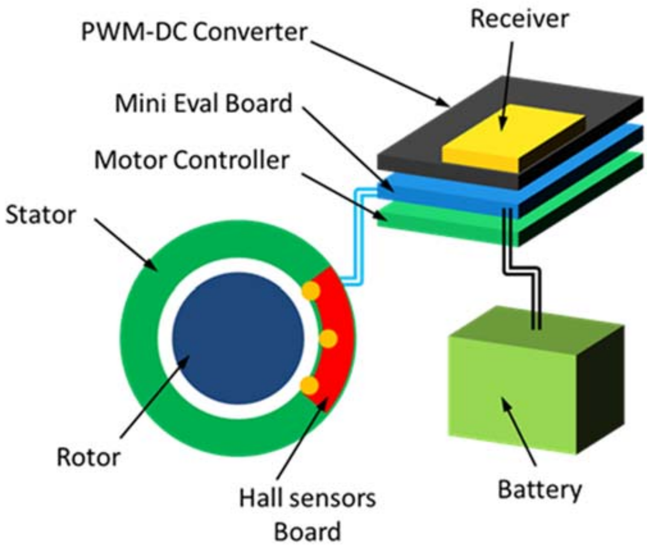

Figure 8-3 Propulsion generator schematics.

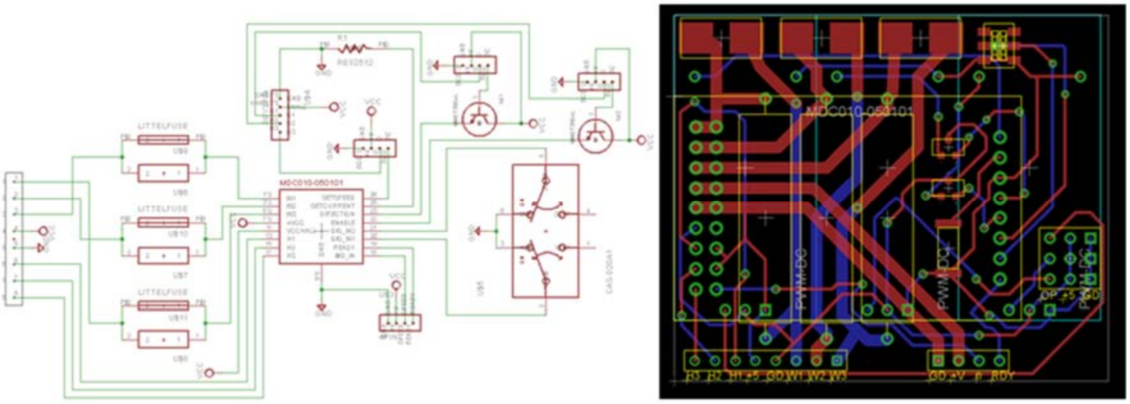

Figure 8-4 Motherboard circuit design using Eagle CAD.

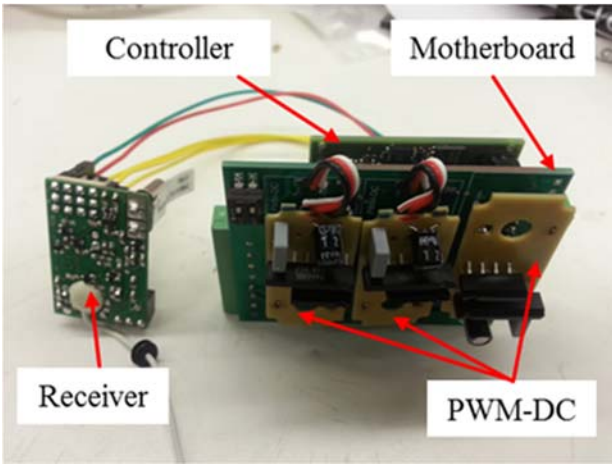

Figure 8-5 Propulsion system electronic ciruit board.

The motor can be controlled wirelessly by an open loop remote controller with three inputs (throttles). The throttles control the power Enable/Disable option, rotor rotation direction (clockwise or counter clockwise) and the rotor speed.

9. CONCOLUSION AND FUTURE WORK

9.1. Conclusion

The major findings and contributions of my thesis are:

1) The underwater vehicle structure was defined to have a torpedo shape with a through-hole (same size of the ring propeller) that permits water flow from the front to the rear. The length of the vehicle was decided to be twice as much the frontal diameter. Therefore, the total volume of the vehicle was constraint with two variables such as the frontal diameter and the ring-propeller diameter. The onboard energy density was taking in to the account along with the vehicle-desired performance to be integrated as constraints to minimize the underwater vehicle outer diameter. Those constraints determined how far the underwater vehicle frontal diameter could be pushed to the minimum without dropping the vehicle performance. It turns out that the smallest underwater vehicle with the specified shape and desired performance to be 6 inches in frontal diameter and 1.6 inches in ring propeller diameter.
2) The size of the miniaturized underwater vehicle was determined. The propulsion system for such a small vehicle size, occupancy and environmental constraint dedicate the urge of designing a custom driving motor to enable vehicle motion. A brushless three-phase DC motor with inrunner rotor permanent magnets was designed and fabricated to have about 3 inches outer diameter and 1.6 inches inner diameter. The air gap diameter was 2.08 inches. The motor can operate in water and rotate at speed of 1200 rpm with the maximum underwater load

providing 30 V power supply. The motor constant was determined numerically and experimentally to be about 0.014.

3) A new technique was developed to pressure house the brushless three-phase DC motor with inrunner rotor permanent magnets. The concept of the design was inspired by the current existing pressure housing method with much simpler structure. The pressure housing prevents the motor electronic circuit components to encounter with the ambient water. A three-dimensional printed pressure housing was built to house the stator winding and its electronics leaving the rotor magnets and the ring propeller to be consistently exposed to water. Several tests were performed on the housing and no leaks were found. The same technique can be modified to enable proper functionality in the seep-sea. An aluminum housing with oil filling will be required to enable deep-sea compatibility.
4) Several types of ring propellers were designed and three-dimensionally printed. Each propeller was designed using blade element theory, which maximizes thrust and efficiency depending on the operating point. A structure with force sensor was built to examine each the brushless three-phase DC motor with each ring propeller. The ring propellers were different in terms of number of blades, pitch or twist angle and blade extensions. After many experiments and testes, I concluded that the ring-propeller with extended three blades and 60^{o} twist angle was the best. The maximum thrust generated was about 3.25 N with a propeller efficiency of 0.46.

9.2. Future work

Although my research built a solid foundation for developing a miniaturized underwater vehicle, still other problems need to be solved before deploying it to the field. For instance, fins are needed to allow vehicle motion in all directions. In addition, a communication method is required to enable vehicle remote controlling. Since the vehicle is designed to carry underwater device measurements, additional communication technique and power sourcing is required which might influence the vehicle overall size and performance. Other future work involve upgrading the vehicle to function in the deep-sea using the proposed pressure housing technique. This constructed pressure housing will function in the deep-sea in order to resist pressures found by ranging up to 3000m deep in the ocean. Finally, design several miniaturized underwater vehicle and enable communication among themselves to perform simultaneously and efficiently to perform a task. For example, several miniaturized underwater vehicles can swim and form node simultaneous measurements.

REFERENCES

Allen, B., Stokey, R., Austin, T., Forrester, N., Goldsborough, R., Purcell, M., & von Alt, C. (1997, October). REMUS: a small, low cost AUV; system description, field trials and performance results. In *OCEANS'97. MTS/IEEE Conference Proceedings* (Vol. 2, pp. 994-1000). IEEE.

Arafat, H. N., Stilwell, D. J., & Neu, W. L. (2006). Development of a dynamic model of a small high-speed autonomous underwater vehicle. *OCEANS 2006,* 1-6.

Atallah, K., Zhu, Z. Q., & Howe, D. (1992). An improved method for predicting iron losses in brushless permanent magnet DC drives. *Magnetics, IEEE Transactions on*, *28*(5), 2997-2999.

Alvarez, A., Caffaz, A., Caiti, A., Casalino, G., Gualdesi, L., Turetta, A., & Viviani, R. (2009). Folaga: A low-cost autonomous underwater vehicle combining glider and AUV capabilities. *Ocean Engineering, 36*(1), 24-38.

Behar, A. E., Bruhn, F. C., & Carsey, F. (2003). Exploring miniaturization limits for an instrumented autonomous submersible explorer for extreme environments. *13th International Symposium on Unmanned Untethered Submersible Technology,*

Bellingham, J. G., Zhang, Y., Kerwin, J. E., Erikson, J., Hobson, B., Kieft, B., . . . Paul, J. (2010). Efficient propulsion for the tethys long-range autonomous underwater vehicle. *Autonomous Underwater Vehicles (AUV), 2010 IEEE/OES,* 1-7.

Bradley, A., Duester, A., Liberatore, S., & Yoerger, D. (2000). Extending the endurance of an operational scientific AUV using lithium-ion batteries. *Proceedings of UUVS,*

Bradshaw, A., Hamacher, T., & Fischer, U. (2011). Is nuclear fusion a sustainable energy form? *Fusion Engineering and Design, 86*(9), 2770-2773.

Briggs, R. C. (2010). *Mechanical Design of a Self-Mooring Autonomous Underwater Vehicle,*

Brown Jr, O., & Hendrick, H. (1986). ROBOTIC VEHICLES: A REVIEW. *Human Factors in Organizational Design and Management-II: Proceedings of the Second Symposium Held in Vancouver, BC, Canada, 19-21 August, 1986, , 2* 29.

Chalk, S. G., & Miller, J. F. (2006). Key challenges and recent progress in batteries, fuel cells, and hydrogen storage for clean energy systems. *Journal of Power Sources, 159*(1), 73-80.

Davis, R. E., Eriksen, C. C., & Jones, C. P. (2002). Autonomous buoyancy-driven underwater gliders. *The Technology and Applications of Autonomous Underwater Vehicles,* , 37-58.

deYoung, B., Heath, M., Werner, F., Chai, F., Megrey, B., & Monfray, P. (2004). Challenges of modeling ocean basin ecosystems. *Science (New York, N.Y.), 304*(5676), 1463-1466. doi:10.1126/science.1094858 [doi]

Dickey, T. D. (1991). The emergence of concurrent high-resolution physical and bio-optical measurements in the upper ocean and their applications. *Reviews of Geophysics, 29*(3), 383-413.

Donovan, G. T. (2012). Position error correction for an autonomous underwater vehicle inertial navigation system (INS) using a particle filter. *Oceanic Engineering, IEEE Journal of, 37*(3), 431-445.

Ekinci, S. (2011). A practical approach for design of marine propellers with systematic propeller series. *Brodogradnja, 62*(2), 123-129.

Eriksen, C. C., Osse, T. J., Light, R. D., Wen, T., Lehman, T. W., Sabin, P. L., . . . Chiodi, A. M. (2001). Seaglider: A long-range autonomous underwater vehicle for oceanographic research. *Oceanic Engineering, IEEE Journal of, 26*(4), 424-436.

Gage, J. D., & Tyler, P. A. (1992). *Deep-sea biology: A natural history of organisms at the deep-sea floor* Cambridge University Press.

Gracias, N., & Santos-Victor, J. (2000). Underwater video mosaics as visual navigation maps. *Computer Vision and Image Understanding, 79*(1), 66-91.

Greig, J., & Sathirakul, K. (1961). Pole-face losses in alternators. an investigation of eddy-current losses in laminated pole shoes. *Proceedings of the IEE-Part C: Monographs, 108*(13), 130-138.

Gundogdu, T., & Komurgoz, G. (2010). Design of permanent magnet machines with different rotor type. *World Academy of Science, Engineering and Technology, 70*

Healey, A. J., Rock, S. M., Cody, S., Miles, D., & Brown, J. P. (1995). Toward an improved understanding of thruster dynamics for underwater vehicles. Oceanic Engineering, IEEE Journal of, 20(4), 354-361.

Holik, P. J., Dorrell, D. G., Lombard, P., Thougaard, H., & Jensen, F. (2006). A multi-sliced finite element model for induction machines incorporating inter-bar current. *Industry Applications Conference, 2006. 41st IAS Annual Meeting. Conference Record of the 2006 IEEE, , 2* 819-826.

Huang, C., Yang, T., Liu, J., & Schindall, J. (2013). Acoustic mapping of ocean currents using networked distributed sensors. *The Journal of the Acoustical Society of America, 134*(3), 2090-2105.

Hyakudome, T., Yoshida, H., Ishibashi, S., Sawa, T., & Nakamura, M. (2011). Development of advanced lithium-ion battery for underwater vehicle. *Underwater Technology (UT), 2011 IEEE Symposium on and 2011 Workshop on Scientific use of Submarine Cables and Related Technologies (SSC),* 1-4.

Hyakudome, T. (2011). Design of autonomous underwater vehicle. *International Journal of Advanced Robotic Systems, 8*(1)

Isern, A., & Clark, H. (2003). The ocean observatories initiative: A continued presence for interactive ocean research. *Marine Technology Society Journal, 37*(3), 26-41.

Islam, R., Husain, I., Fardoun, A., & McLaughlin, K. (2009). Permanent-magnet synchronous motor magnet designs with skewing for torque ripple and cogging torque reduction. *Industry Applications, IEEE Transactions on, 45*(1), 152-160.

Jahnke, R. A., & Christiansen, M. B. (1989). A free-vehicle benthic chamber instrument for sea floor studies. Deep Sea Research Part A. Oceanographic Research Papers, 36(4), 625-637.

Karl, T. R., & Trenberth, K. E. (2003). Modern global climate change. *Science (New York, N.Y.), 302*(5651), 1719-1723. doi:10.1126/science.1090228 [doi]

Kennedy, G. C., & Holt, J. K. (1995). Developing a high efficiency means of propulsion for underwater vehicles. *Southcon/95. Conference Record,* 352-356.

Kim, S., Choi, H., Lee, J., & jun Lee, Y. (2014). Design, implementation, and experiment of an underwater robot for effective inspection of underwater structures. *Robot intelligence technology and applications 2* (pp. 821-829) Springer.

Korgen, B. J., Bodvarsson, G., & Kulm, L. (1970). Current speeds near the ocean floor west of oregon. *Deep Sea Research and Oceanographic Abstracts, , 17*(2) 353-357.

Koss, M., Booth, T., & Sullo, K.On the measurement of the characteristic rotation decay time for a baseball.

Larsen, M. B. (2000). Synthetic long baseline navigation of underwater vehicles. *OCEANS 2000 MTS/IEEE Conference and Exhibition, , 3* 2043-2050.

Lloret, J., Sendra, S., Ardid, M., & Rodrigues, J. J. (2012). Underwater wireless sensor communications in the 2.4 ghz ism frequency band. *Sensors, 12*(4), 4237-4264.

Lopez-de-Heredia, A., Calleja, C., Lertxundi, A., Aranburu, A., & Nieva, T. (2011). Stator current and power factor optimization in an IPMSM for railway traction application. *Power Electronics and Applications (EPE 2011), Proceedings of the 2011-14th European Conference on,* 1-10.

Maier-Reimer, E., & Hasselmann, K. (1987). Transport and storage of CO2 in the ocean——an inorganic ocean-circulation carbon cycle model. *Climate Dynamics, 2*(2), 63-90.

Manwel, J., McGowan, J., & Rogers, A. (2002). Wind energy explained.

Martin, S. C., Whitcomb, L. L., Yoerger, D., & Singh, H. (2006). A mission controller for high level control of autonomous and semi-autonomous underwater vehicles. *OCEANS 2006,* 1-6.

Matuszewski, L., & Falkowski, K. (2003). Ring thruster with magnetic bearings. *OCEANS 2003. Proceedings, , 4* 2023-2031.

Mavor, J. W., Froehlich, H. E., Marquet, W. M., & Rainnie, W. O. (1967). *Alvin, 6000-ft. submergence research vehicle* Woods Hole Oceanographic Institution.

Murakami, H., Kataoka, H., Honda, Y., Morimoto, S., & Takeda, Y. (2001). Highly efficient brushless motor design for an air-conditioner of the next generation 42 V vehicle. *Industry Applications Conference, 2001. Thirty-Sixth IAS Annual Meeting. Conference Record of the 2001 IEEE, , 1* 461-466.

Okamoto, M., Yasuda, K., & Azuma, A. (1996). Aerodynamic characteristics of the wings and body of a dragonfly. *The Journal of Experimental Biology, 199*(Pt 2), 281-294.

Petrich, J., & Stilwell, D. J. (2011). Robust control for an autonomous underwater vehicle that suppresses pitch and yaw coupling. *Ocean Engineering, 38*(1), 197-204.

Pivano, L., Johansen, T., Smogeli, O., & Fossen, T. (2007). Nonlinear thrust controller for marine propellers in four-quadrant operations. *American Control Conference, 2007. ACC'07,* 900-905.

Poole, P. K., & Clower, P. (1996). A systems approach to autonomous underwater vehicle (AUV) propulsion design. *Marine Technology Society Journal, 30*(2), 8-16.

Post, R. S. (1999). Permanent magnet coupling fundamentals. *AISE steel technology*, *76*, 54-58.

Prestero, T. T. J. (2001). *Verification of a Six-Degree of Freedom Simulation Model for the REMUS Autonomous Underwater Vehicle,* Ramírez, J. A., Vásquez, R. E., Gutiérrez, L. B., & Flórez, D. A. (2007). Mechanical/Naval design of an underwater remotely operated vehicle (ROV) for surveillance and inspection of port facilities. *ASME 2007 International Mechanical Engineering Congress and Exposition,* 351-361.

Rowe, F., & Young, J. (1979). An ocean current profiler using doppler sonar. *OCEANS'79,* 292-297.

Ruiz, S., Garau, B., Martínez-Ledesma, M., Casas, B., Pascual, A., Vizoso, G., . . . Testor, P. (2012). New technologies for marine research: 5 years of glider activities at IMEDEA-TMOOS. *Scientia Marina, 76*(S1), 261-270.

Sasdelli, K. R., & Spargo, J. D. (1971). *Rotary Shaft Seal Selection Handbook for Pressure-Equalized, Deep-Ocean Equipment* (No. NSRDL/A-7-573). NAVAL SHIP RESEARCH AND DEVELOPMENT LABANNAPOLIS MD.

Schelleng, J., Burrows, C., & Ferrell, E. (1933). Ultra-short-wave propagation. *Radio Engineers, Proceedings of the Institute of, 21*(3), 427-463.

Schubel, P. J., & Crossley, R. J. (2012). Wind turbine blade design. *Energies, 5*(9), 3425-3449.

Shaneyfelt, T., Joordens, M. A., Nagothu, K., & Jamshidi, M. (2008). RF communication between surface and underwater robotic swarms. *WAC'08: Proceedings of the World Automation Congress' 08,* 1-6.

Sharkh, S. A., Lai, S. H., & Turnock, S. (2004). Structurally integrated brushless PM motor for miniature propeller thrusters. *IEE Proceedings-Electric Power Applications, 151*(5), 513-519.

Shen, Q., Wang, T., Liang, J., & Wen, L. (2013). Hydrodynamic performance of a biomimetic robotic swimmer actuated by ionic polymer–metal composite. *Smart Materials and Structures, 22*(7), 075035.

Singh, H., Yoerger, D., & Bradley, A. (1997). Issues in AUV design and deployment for oceanographic research. *Robotics and Automation, 1997. Proceedings., 1997 IEEE International Conference on, , 3* 1857-1862.

Stamenkovic, I., Milivojevic, N., Schofield, N., Krishnamurthy, M., & Emadi, A. (2013). Design, analysis, and optimization of ironless stator permanent magnet machines. *Power Electronics, IEEE Transactions on, 28*(5), 2527-2538.

Takeuchi, J., Miraghaie, R., Yuki, K., Satake, S., Kunugi, T., & Morley, N. (2003). Turbulent velocity profile measurement in circular pipe flow using particle image velocimetry technique. *Fusion Engineering, 2003. 20th IEEE/NPSS Symposium on,* 140-143.

Tivey, M. A., & Johnson, H. P. (1990). The magnetic structure of axial seamount, juan de fuca ridge. *Journal of Geophysical Research: Solid Earth (1978–2012), 95*(B8), 12735-12750.

Tonder, K., & Salant, R. (1992). Non-leaking lip seals: a roughness effect study.*Journal of tribology*, *114*(3), 595-599.

Tunnicliffe, V. (1992). Hydrothermal-vent communities of the deep sea. *American Scientist,* , 336-349.

Tyson, F. L., Rice, D. L., & Dearry, A. (2004). Connecting the oceans and human health. *Environmental Health Perspectives, 112*(8), A455-6.

Vasilescu, I., Varshavskaya, P., Kotay, K., & Rus, D. (2005). Autonomous modular optical underwater robot (amour) design, prototype and feasibility study. *Robotics and Automation, 2005. ICRA 2005. Proceedings of the 2005 IEEE International Conference on,* 1603-1609.

von Alt, C. (2003). Autonomous underwater vehicles. *Autonomous Underwater Lagrangian Platforms and Sensors Workshop, , 3*

Watson, S. A., & Green, P. N. (2010). Propulsion systems for micro-autonomous underwater vehicles (μAUVs). *Robotics Automation and Mechatronics (RAM), 2010 IEEE Conference on,* 435-440.

Winter, M., & Brodd, R. J. (2004). What are batteries, fuel cells, and supercapacitors? *Chemical Reviews, 104*(10), 4245-4270.

Witze, A. (2013). Marine science: Oceanography's billion-dollar baby. *Nature, 501*(7468), 480-482. doi:10.1038/501480a [doi]

Yakovlev, A. Y., Sokolov, M. A., & Marinich, N. V. (2011). Numerical design and experimental verification of a RIM-driven thruster. *Proceedings of Second International Symposium on Marine Propulsors. Hamburg, Germany,*

Yang, Z., Zhang, J., Kintner-Meyer, M. C., Lu, X., Choi, D., Lemmon, J. P., & Liu, J. (2011). Electrochemical energy storage for green grid. *Chemical Reviews, 111*(5), 3577-3613.

Yeadon, W. H., & Yeadon, A. W. (Eds.). (2001). *HB SMALL ELECTRIC MOTORS, 1.* McGraw Hill Professional.

Yildiz, O., Yilmaz, A. E., & Gokalp, B. (2009). State-of-the-art system solutions for unmanned underwater vehicles. *Sensors, 1*, 2.

Yoerger, D. R., Jakuba, M., Bradley, A. M., & Bingham, B. (2007). Techniques for deep sea near bottom survey using an autonomous underwater vehicle. *The International Journal of Robotics Research, 26*(1), 41-54.

Yoerger, D. R., & Newman, J. B. (1986). Jason: An integrated approach to rov and control system design. *ROV'86: Remotely operated vehicles* (pp. 340-353) Springer.

Yoerger, D. R., Newman, J., & Slotine, J. (1986). Supervisory control system for the jason rov. *Oceanic Engineering, IEEE Journal of, 11*(3), 392-400.

Yoerger, D. R., Von Alt, C. J., Bowen, A. D., & Newman, J. (1986). Design of underwater vehicles for high performance control. *OCEANS'86,* 1431-1437.

Yoerger, D., Bradley, A., Martin, S., & Whitcomb, L. (2006). The sentry autonomous underwater vehicle: Field trial results and future capabilities. *AGU Fall Meeting Abstracts, , 1* 1674.

Yuh, J. (2000). Design and control of autonomous underwater robots: A survey. *Autonomous Robots, 8*(1), 7-24.

Yuh, J., Choi, S., Ikehara, C., Kim, G., McMurty, G., Ghasemi-Nejhad, M., . . . Sugihara, K. (1998). Design of a semi-autonomous underwater vehicle for intervention missions (SAUVIM). *Underwater Technology, 1998. Proceedings of the 1998 International Symposium on,* 63-68.

APPENDIX A

mUV OPTIMAL MOTION TRAJECTORY

The mUV nonlinear system composed of two inputs (u_1 and u_2), six state variables (x_1 to x_6) and six outputs (x_1 to x_6) as it was mentioned in Equation (4.16). Assuming a scenario where the mUV starting from rest at an initial position (x_0, y_0) and a yaw angle θ_0 , then swims and comes to rest after t_f time at (x_f, y_f) position with a yaw angle θ_f . An optimal trajectory can be calculated to drive the mUV from one place to another with some specific initial conditions and final conditions while minimizing the inputs. Therefore, a cost function *J* can be created for the variable that I want to minimize.

$$J = \sum_{i=1}^{6} \left\{ F_i\left[x_i(t_0) - x_{i0}\right]^2 + F_{i+6}\left[x_i(t_f) - x_{if}\right]^2 \right\} + \int_{to}^{tf} \left[ru_1^2(t) + ru_2^2(t)\right]dt \,. \tag{A.1}$$

From the cost function, the Hamiltonian function *H* can be derived.

$$H = ru_1^2(t) + ru_2^2(t) + \sum_{i=1}^{6} \lambda_i \dot{x}_i \,. \tag{A.2}$$

The rate of change of λ_i can be determined by taking the negative derivative of the Hamiltonian equation with respect to x_i .

$$\begin{aligned}
\dot{\lambda}_1 &= 2a_{12}x_1\lambda_1 - 2b_{31}x_1u_2\lambda_3 - \cos(x_4)\lambda_5 - \sin(x_4)\lambda_6 \\
\dot{\lambda}_2 &= -a_{11}x_2\lambda_1 + a_{21}\lambda_2 + 2a_{22}x_2\lambda_2 \\
\dot{\lambda}_3 &= a_{31}\lambda_3 - \lambda_4 + a_{51}\sin(x_4)\lambda_5 - a_{51}\cos(x_4)\lambda_6 \\
\dot{\lambda}_4 &= x_1\sin(x_4)\lambda_5 + a_{51}x_3\cos(x_4)\lambda_5 - x_1\cos(x_4)\lambda_6 + a_{51}x_3\sin(x_4)\lambda_6 \\
\dot{\lambda}_5 &= 0 \\
\dot{\lambda}_6 &= 0
\end{aligned} \,. \tag{A.3}$$

The inputs u_i can be determined by making the derivative of the Hamiltonian with respect to u_i equal to zero.

$$\left.\begin{aligned} 2ru_1 + b_{21}\lambda_2 = 0 \\ 2ru_2 + b_{31}x_1|x_1|\lambda_3 = 0 \end{aligned}\right\}. \tag{A.4}$$

The ODEs described in equations (4.16), (A.3) and (A.4) can be used to solve for the necessary inputs u_i.

A MATLAB code was generated to solve the optimal trajectory problem with the initial and final conditions described in Table A–1. The code solves the ODE sets by iteration going from forward and backward in time.

Table A–1

Optimal trajectory example initial and final conditions

Variable	Initial time (0 sec)	Final time (300 sec)
mUV speed (x_1)	0	0
Propeller speed (x_2)	0	0
mUV yaw speed (x_3)	0	0
mUV yaw angle (x_4)	0°	0°
mUV *x* location (x_5)	0	80 m
mUV *y* location (x_6)	0	50 m

After about 400 iterations (18 hours), the solution converges with an error near 10^{-5} (see Figure A-1).

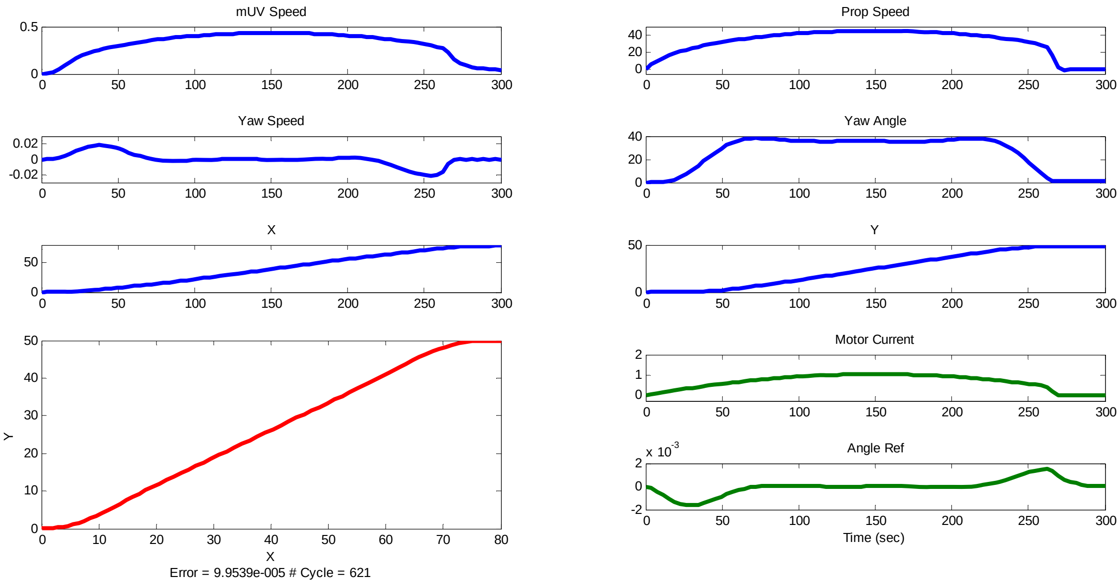

Figure A-1 MATLAB results of the optimal trajectory example of the mUV going from initial position to the final position in 300 sec.

The MATLAB code is composed of three .m files.

ODE_L.m MATLAB file

```
function dL = ODE_L(t,L,tu,x,u,A,B)

a11 = A(1);

a12 = A(2);

a21 = A(3);

a22 = A(4);

a31 = A(5);

a51 = A(6);

b21 = B(1);
```

```
b31 = B(2);

u(1) = spline(tu,u(:,1),t);

u(2) = spline(tu,u(:,2),t);

x(1) = spline(tu,x(:,1),t);

x(2) = spline(tu,x(:,2),t);

x(3) = spline(tu,x(:,3),t);

x(4) = spline(tu,x(:,4),t);

x(5) = spline(tu,x(:,5),t);

x(6) = spline(tu,x(:,6),t);

dL = zeros(6,1);

dL(1) = 2*a12*x(1)*L(1) + 2*b31*x(1)*u(2)*L(3) - L(5)*cos(x(4)) - L(6)*sin(x(4));

dL(2) = -2*a11*x(2)*L(1) + a21*L(2) + 2*a22*x(2)*L(2);

dL(3) = a31*L(3) - L(4) + a51*sin(x(4))*L(5) - a51*cos(x(4))*L(6);

dL(4) = x(1)*L(5)*sin(x(4)) - x(1)*L(6)*cos(x(4)) + a51*x(3)*cos(x(4))*L(5) +

a51*x(3)*sin(x(4))*L(6);

dL(5) = 0;

dL(6) = 0;
```

ODE_x.m MATLAB file

```
function dx = ODE_x(t,x,tu,u,A,B)

a11 = A(1);
a12 = A(2);

a21 = A(3);
```

```
a22 = A(4);
a31 = A(5);
a51 = A(6);
b21 = B(1);
b31 = B(2);
u(1) = spline(tu,u(:,1),t);
u(2) = spline(tu,u(:,2),t);
dx = zeros(6,1);
dx(1) = a11*x(2)*abs(x(2)) - a12*x(1)*abs(x(1));
dx(2) = - a21*x(2) - a22*x(2)*abs(x(2)) + b21*u(1);
dx(3) = - a31*x(3) - b31*x(2)*abs(x(2))*u(2);
dx(4) = x(3);
dx(5) = x(1)*cos(x(4)) - a51*x(3)*sin(x(4));
dx(6) = x(1)*sin(x(4)) + a51*x(3)*cos(x(4));
```

Solver.m MATLAB file

```
clear;clc;close all
GetU;
S = figure(1);
set(S,'Position',[50 60 1200 600]);
rho = 1000;
Cd = 0.267;
```

```
m = 3.77;
A = pi*(3*.0254)^2;
p = .0082;
b = 1.42e-4;
N = 0.0232;
J = 0.00011538;
Ct = 0.0771;
Cq = 0.0797;
d = 1.625*.0254;
l = .5;
k = .0245;
a11 = Ct*rho*d^4/m;
a12 = rho*Cd*A/(2*m);
a21 = b/J;
a22 = Cq*rho*d^5/J;
b21 = k/J;
a31 = l/N;
b31 = p/N;
a51 = 5*.0254;
A = [a11 a12 a21 a22 a31 a51];
B = [b21 b31];
tu = linspace(t0,tf,M);
```

```
u(:,1) = -4.2/tf^2*tu.^2+4.2/tf*tu;

u(:,2) = zeros(M,1);

x0 = [0 0 0 theta0 x0 y0];

ER = 1e-20;

err = 1;

w = 5;

I = 1;

while err>ER

   [TX,X] = ode23s(@(t,x) ODE_x(t,x,tu,u,A,B),[t0 tf],x0);

   XX(:,1) = spline(TX,X(:,1),tu);

   XX(:,2) = spline(TX,X(:,2),tu);

   XX(:,3) = spline(TX,X(:,3),tu);

   XX(:,4) = spline(TX,X(:,4),tu);

   XX(:,5) = spline(TX,X(:,5),tu);

   XX(:,6) = spline(TX,X(:,6),tu);

   Lambda1tf = F1*(XX(end,1));

   Lambda2tf = F2*(XX(end,2));

   Lambda3tf = F3*(XX(end,3));

   Lambda4tf = F4*(XX(end,4)-thetaf);

   Lambda5tf = F5*(XX(end,5)-xf);

   Lambda6tf = F6*(XX(end,6)-yf);

   clear U
```

```
    U(:,1) = spline(tu',u(:,1),TX);
    U(:,2) = spline(tu',u(:,2),TX);
    [TL,Lam] = ode23s(@(t,L) ODE_L(t,L,TX,X,U,A,B),[tf t0],[Lambda1tf Lambda2tf
Lambda3tf Lambda4tf Lambda5tf Lambda6tf]);
    Lambda(:,1) = spline(TL,Lam(:,1),tu);
    Lambda(:,2) = spline(TL,Lam(:,2),tu);
    Lambda(:,3) = spline(TL,Lam(:,3),tu);
    Lambda(:,4) = spline(TL,Lam(:,4),tu);
    Lambda(:,5) = spline(TL,Lam(:,5),tu);
    Lambda(:,6) = spline(TL,Lam(:,6),tu);
    dHdu1 = 2*r1*u(:,1) + b21*Lambda(:,2);
    dHdu2 = 2*r2*u(:,2) - b31*Lambda(:,3).*XX(:,2).*abs(XX(:,2));
    u1_new = u(:,1) - EPS*dHdu1;
    u2_new = u(:,2) - EPS*dHdu2;
    err = max(abs(u(:,1)-u1_new))+max(abs(u(:,2)-u2_new));
    u(:,1) = u1_new;
    u(:,2) = u2_new;
    if w >= 0
        subplot(5,2,1)
        plot(tu,XX(:,1))
        title('mUV Speed')
        subplot(5,2,2)
```

```
plot(tu,XX(:,2))

title('Prop Speed')

subplot(5,2,3)

plot(tu,XX(:,3))

title('Yaw Speed')

subplot(5,2,4)

plot(tu,XX(:,4)*180/pi)

title('Yaw Angle')

subplot(5,2,5)

plot(tu,XX(:,5))

title('X')

subplot(5,2,6)

plot(tu,XX(:,6))

title('Y')

subplot(5,2,[7,9])

plot(XX(:,5),XX(:,6))

xlabel({'X';['Error = ' num2str(err) ' # Cycle = ' num2str(I)]})

ylabel('Y')

subplot(5,2,8)

plot(tu,u(:,1))

title('Motor Current')

subplot(5,2,10)
```

```
        plot(tu,u(:,2))

        title('Angle Ref')

        drawnow

        w = 0;

        I = I + 1;

    end

    w = w + 1;

end
```

GetU.m MATLAB file

```
F1 = 1000000;

F2 = 10;

F3 = 1;

F4 = 10000;

F5 = 50; %X

F6 = 30; %Y

r1 = 1;

r2 = 0.001;

M = 80;

EPS = 1e-10;

t0 = 0;

tf = 300;
```

```
x0 = 0;

y0 = 0;

xf = 80;

yf = 50;

theta0 = 10*pi/180;

thetaf = 50*pi/180;
```

APPENDIX B

FRONTAL DRAG OF THE mUV

The drag coefficient C_D of the vehicle can be calculated using the drag force equation. In a laminar flow, the drag coefficient can depend only on the Reynolds's Number Re; wind tunnel test is usually the comment method to determine the drag force acting on a body exposed to a wind speed u. However, in order to match the aerodynamic property of the simulation, the Reynolds's Number Re of the flow using water as fluid and water speed of 1 m/s was calculated. In that laminar flow the wind, speed was determined using the same Re and air thermodynamic properties. The wind speed is about 15.25 times higher than the water current speed (see Figure B-2).

The experiment was performed at Arizona State University in the mechanical engineering wind tunnel facility. The experimental data are plotted in Figure B-3, which shows as expected a linear relation between the dynamic pressure and the drag pressure.

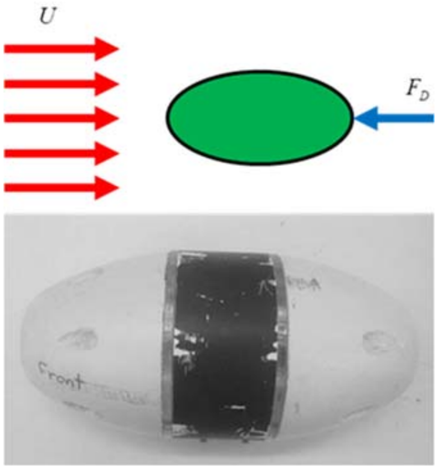

Figure B-2 Schematics of the experimental setup.

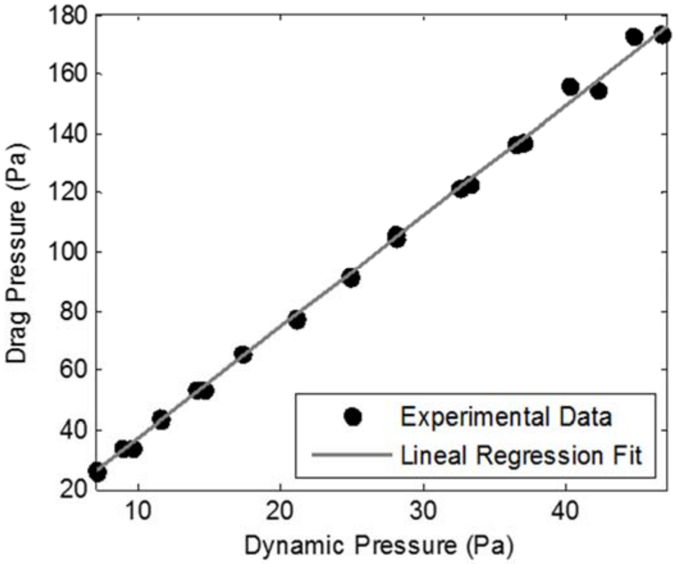

Figure B-3 Experimental Data of the AUV drag pressure vs. dynamic pressure. The equation of the linear regression fit for this data is $P_{drag} = 3.75\ P_{dyn}$. The measured frontal drag coefficient of the mUV is 0.267.